Title:
Rectangular drainage pattern evolution controlled by pipe cave collapse along clastic dikes, the Dead Sea Basin, Israel

Authors:
Liran Goren[1,*], Matanya Hamawi[1,2], Amit Mushkin[2], Tsafrir Levi[2]

Affiliations:
[1]Department of Earth and Environmental Sciences, Ben Gurion University of the Negev, Beer Sheva, Israel
[2]The Geological Survey of Israel, Jerusalem, Israel

Corresponding author: Liran Goren, gorenl@bgu.ac.il

Rectangular drainage pattern evolution controlled by pipe cave collapse along clastic dikes, the Dead Sea Basin, Israel

Liran Goren[1,*], Matanya Hamawi[1,2], Amit Mushkin[2], Tsafrir Levi[2]

[1]Department of Earth and Environmental Sciences, Ben Gurion University of the Negev, Beer Sheva, Israel

[2]The Geological Survey of Israel, Jerusalem, Israel

[*]Corresponding author contact details: gorenl@bgu.ac.il

Abstract

Rectangular drainage networks are characterized by right-angle bends and confluences. The formation of such patterns is commonly associated with orthogonal sets of fractures, making them an outstanding example for structurally controlled landform evolution. However, this association remains largely circumstantial because little is known about how rectangular drainages mechanistically link to orthogonal fractures. We investigated these linkages in the hyper-arid Ami'az Plain located within the Dead Sea Basin in Israel. The Ami'az Plain is incised by a rectangular canyon system and is penetrated by hundreds of sub-vertical clastic dikes (mode-I fractures infilled with sediments). Numerous caves extend from the banks and heads of the canyon system. Based on field surveys and analysis of a high-resolution LiDAR data, we mapped the Ami'az Plain drainage network and its associated geomorphic landforms including sinkholes. Our analysis revealed that the subaerial tributaries of the canyon system share dominant orientations with the strike of the clastic dikes. In addition, subsurface mapping assisted by Ground scanning LiDAR, together with field experiments, demonstrated that the caves and sinkholes in the Ami'az Plain are spatially associated with clastic dikes and that the caves formed by piping erosion along dikes. Based on these findings, we suggest that clastic dikes act as efficient infiltration pathways to the subsurface, and subsurface flow along clastic dikes induces internal erosion that forms pipe caves. The sinkholes form by collapses of cave roofs. Coalescence of sinkholes and seepage erosion where dikes intersect canyon heads generate new tributaries and act to extend existing ones. Fluvial erosion and bank collapse modify the drainage network. Our findings emphasize the critical role of subsurface erosion, caves and sinkholes in linking fractures to drainage pattern evolution, and provide new process-based framework to interpret rectangular drainage networks on Earth and other planetary surfaces.

Keywords: drainage pattern, rectangular pattern, clastic dikes, piping caves, internal erosion, piping erosion, seepage erosion, sinkholes.

1 Introduction

Fluvial drainage patterns refer to the plan-view geometry of basin flowlines. Common drainage patterns include (but are not limited to): dendritic, parallel, trellis, radial and rectangular (Campbell, 1896; Zernitz, 1932; Howard, 1967; Deffontaines and Chorowicz, 1991; Ichoku and Chorowicz, 1994; Mejía and Niemann, 2008; Jung et al., 2017). The evolution of such drainage patterns over geological timescales is driven by geomorphic processes and their respond to regional drivers, such as lithology, slope distribution, and geologic fabric and structures including folds, faults, and joints (Howard, 1967; Abrahams and Flint, 1983; Argialas et al., 1988; Deffontaines and Chorowicz, 1991; Twidale, 2004).

Rectangular drainage patterns are characterized by right-angle flowline bends and channel confluences (e.g., Zernitz, 1932). The formation of rectangular drainages has been association with orthogonal joints and faults (Zernitz, 1932; Howard, 1967; Deffontaines and Chorowicz, 1991), and therefore presents an exceptional example for landform evolution controlled by pre-existing geologic structures. Well-studied examples of rectangular drainages include the Adirondack Mountains, NY, USA (Kemp, 1894; Zernitz, 1932; Deffontaines and Chorowicz, 1991; Mejía and Niemann, 2008; Jung et al., 2015, 2017, 2019) (Figure 1a), which was suggested to be controlled by an orthogonal system of normal faults (Kemp, 1894), and sections of the Zambezi river in Zimbabwe and Zambia (Zernitz, 1932; Twidale, 2004), where orthogonal systems of both joints and faults dominate the landscape. Rectangular drainages have also been documented on Venus (Komatsu et al., 2001; Khawja et al., 2020), Mars (Figure 1c), and Titan (Burr et al., 2009, 2013)(Figure 1d), where links to sets of fractures (joints and faults) remain speculative. While the spatial associations of fracture systems with rectangular drainages are widely documented in terrestrial settings, the structural control remains circumstantial because the mechanistic linkage between structures and rectangular drainages remains poorly constrained.

Irrespective of rectangular drainages, spatial and mechanistic linkages between fractures and streams have been extensively discussed (e.g. Whipple et al., 2000b; Molnar et al., 2007; Pelletier et al., 2009; Anton et al., 2015). A recent review by Scott and Wohl (2019) emphasized the effect of dense fracture systems on focused erosion, whereby dense fractures facilitate plucking and increase the susceptibility to chemical weathering, leading to localized fluvial erosion where fracture density increases. As an outcome, fracture-induced spatial variability in erodibility tends to form streams that follow the path of the heavily damaged region, or follow the trend of large fractures in a set (Whipple et al., 2000a; Pelletier and Baker, 2011; Roy et al., 2015; Duvall et al., 2020).

Fractures could also act as preferential subsurface flow pathways, inducing erosion at the subsurface and prescribing the course of flowlines (Dunne, 1980; Dunne et al., 1990). More specifically, the collapse of pipe caves formed by *internal erosion* (Nieber et al., 2013) forms gullies along hillslopes (Parker and Higgins, 1990; Zhu, 2012; Bernatek-Jakiel and Wrońska-Wałach, 2018), and *seepage erosion* gradually undermines channel heads and promotes headward retreat (Pillans, 1985; Schumm and Phillips, 1986; Schumm et al., 1995; Nieber et al., 2013; Micallef et al., 2020). While these processes can occur without any association with fractures, in fractured terrains, the tendency of fractures to focus subsurface flow accentuates their role in inducing subsurface erosion (Dunne, 1980; Dunne et al., 1990). Subaerial flow systems that develop in such settings, commonly follow the subsurface system and the course of the fractures (Dunne, 1980; Laity and Malin, 1985; Farifteh and Soeters, 1999; Lazzari

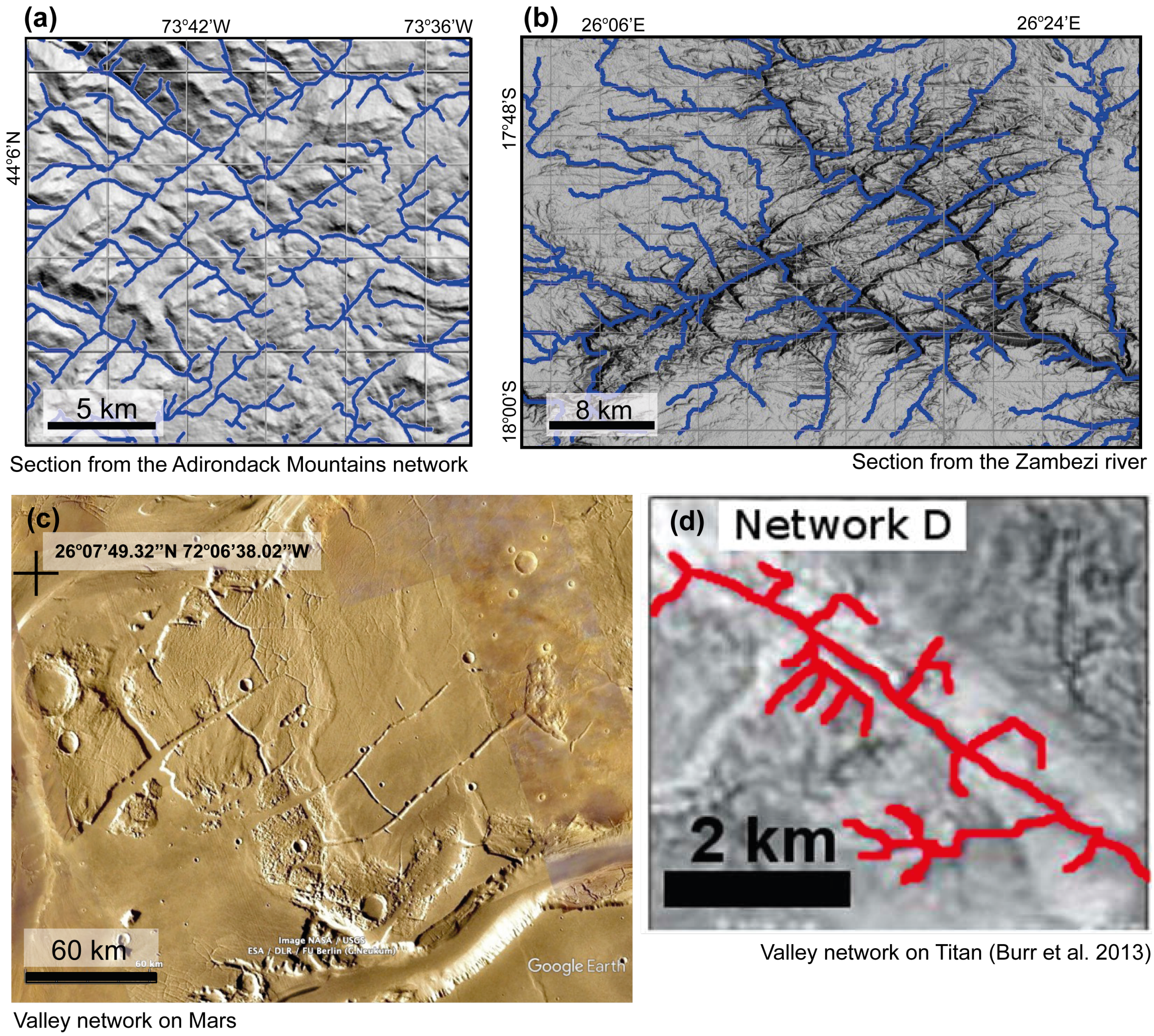

Figure 1: Examples of terrestrial and planetary rectangular networks. (a) A section of the Adirondack Mountains, NY, USA drainage netwrok. (b) A section of the Zambezi river at the border of Zimbabwe and Zambia. (c) A rectangular valley network on Mars. (d) A rectangular drainage system on Titan, following Burr et al. (2013).

et al., 2006).

Although the studies mentioned above did not specifically address the formation and evolution of rectangular drainage networks, they imply that subsurface erosion along orthogonal fracture sets could be a significant process associated with rectangular drainages. This, in turn, could suggest that rectangular drainages may reflect not only their structural origin (Burr et al., 2013), but also the possibility of a system of subsurface cavities associated with the subaerial rectangular pattern, with critical implications for surface collapse hazards and for the search of caves in rocky planets.

In the present study, we use a natural field laboratory to explore the mechanistic association between orthogonal fracture sets, subsurface erosion, and the evolution of a rectangular Holocene drainage network. The studied area is located in Ami'az Plain, within the Dead Sea Basin in Israel (Figure 2), where arial photos suggest presence of a rectangular drainage pattern. Previous studies in the Ami'az Plain (Marco et al., 2002; Levi et al., 2006a,b, 2011; Jacoby et al., 2015) documented hundreds of clastic dikes (subvertical mode-I opening fractures infilled by sediments) as well as a widespread system of caves and cavities (Levi et al., 2014). The good exposure of geologic structures and geomorphic landforms in Ami'az Plain makes this study area an outstanding site for exploring process-based linkages between geologic fractures, drainage patterns, and subsurface cave systems. Towards this goal, we quantified the rectangular characteristics of the Pratzim drainage netwrok (Figure 2) and conducted fieldwork to investigate relations between the drainage network, clastic dikes and caves. Based on our findings, we propose a hydrologic-geomorphic model that explains how dikes and caves drive the evolution of the Ami'az Plain rectangular drainage pattern.

2 Study area

The Ami'az Plain is an approximately two km wide by four km long basin with an exceptionally planar surface that lies to the west of the southern Dead Sea (Figure 2). The Ami'az Plain is located within a down-faulted hanging block of a western segment of the Dead Sea Fault System, which forms the boundary between the Arabian plate and the Sinai subplate (Garfunkel et al., 1981; Marco et al., 2005) (Figure 2). The footwall block, to the west of Ami'az Plain is built of dolomite and limestone rocks of the Upper Cretaceous Judea group, and it reaches an elevation of 140 m above sea level, rising approximately 390 m above Ami'az Plain. To the east, the Ami'az Plain is bounded by Mount Sedom salt diapir and the Sedom Fault. Mount Sedom, which is capped by a veneer of Late Quaternary sediments, reaches an elevation of 160 below sea level (bsl) and rises $\sim$90 m above Ami'az Plain (Zak and Freund, 1980; Weinberger et al., 2006a,b, 2007; Sneh and Weinberger, 2014). Wadi Bki'im and Wadi Ami'az bound the study area from north and south, respectively. The Ami'az Plain is drained by an ephemeral canyon system of Wadi Pratzim, which flows northward into the Dead Sea. The total drainage area of Wadi Pratzim at the northern point of the study area is 14.4 km^2, and it consists of the southern and central sections of Ami'az Plain itself together with the western slopes of Mount Sedom (11.1 km^2) and of a smaller area (3.3 km^2) at the foothills of Judea mountains along the proximal footwall block.

Lithology. The Ami'az Plain consists of a late Pleistocene $\sim$40 m thick sequence of sediments, belonging to the Lisan formation (Marco et al., 2002; Haase-Schramm et al., 2004; Levi

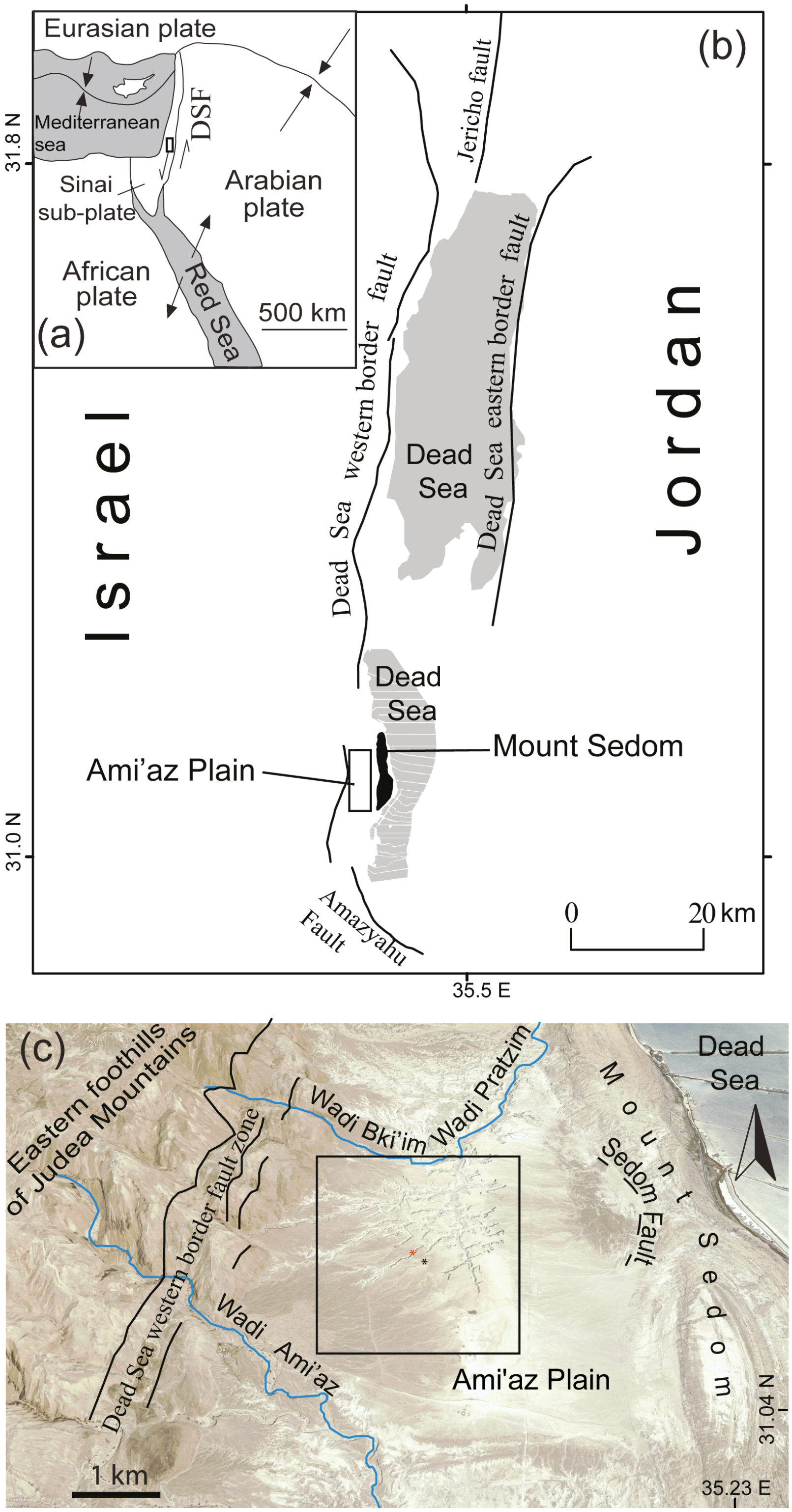

Figure 2: (a) Regional tectonic setting of Arabia-Sinai plate boundary and the eastern Mediterranean. (b) Major segments of the Dead Sea Fault System near the study area following Sneh and Weinberger (2014). (c) Google Earth image with regional structures. The black polygon marks the study area in the Ami'az Plain. Red and black asterisks mark the lower and upper entrances to the Flour Cave, respectively.

et al., 2006a,b). The Lisan formation consists of lacustrine alternating varves of authigenic aragonite and transported fine particles detritus of dolomite, calcite, gypsum, and quartz, as well as kaolinite, illite and montmorillonite clay minerals (Arkin and Michaeli, 1986). The lowest member, approximately 5 m thick, contains alternating varves interbedded with three discrete gypsum layers. In places, thick green, clay-rich layers are exposed at the base of the member. The middle member, approximately 25 m thick, consists of alternating varves interbedded with clastic sand, silt, and clay layers, and a few gypsum sub-layer. The upper member, approximately 10 m thick, consists of alternating varves and ∼1.5 m thick gypsum layer at the top. In some outcrops, the upper gypsum layer is interbedded with the alternating varves. The upper gypsum layer builds the surface of Ami'az Plain, and a thin veneer (<1 m) of eolian, colluvial, and alluvial sediments overlies the formation and covers the surface.

Clastic Dikes. The Lisan formation in the Ami'az Plain is penetrated by hundreds of clastic dikes, which are well exposed at the canyon walls of Wadi Pratzim. Most of the dikes are infilled by injected material composed of green clay, silty quartz, and some aragonite fragments. In the upper parts, the dikes are sometimes filled by brownish silt which resembles the material from the capping surface sediments. Dike heights vary between 5 mm and 18 m, and dike opening varies between 1 mm and 0.18 m. The opening of the long dikes (height > 10 m) is generally greater than 7 mm (Levi et al., 2011). Most of the dikes terminate at the upper gypsum layer, but some penetrate it and reach the surface. Levi et al. (2006b, 2011) proposed that most of the injection dikes were formed during co-seismic loading that caused pressure buildup within a detritus source layer. The high pressure induced fluidization and the propagation of pressure-driven fracture ahead of the injected clastic material that consequently filled the fractures.

Climate. The climate in the study area is hyper arid. Based on the Sedom station of the Israel Meteorological Service, located 6 km southeast of the study area, the average daily temperature ranges between 17.1°C in January and 35.6°C in July and the average annual precipitation is 41.1 mm. The average number of rainy days per year is 8.3 and 2.2 days, considering thresholds of 1 and 5 mm per day, respectively. Importantly, not all rain events induce runoff.

Caves. Levi et al. (2014) identified many caves and subsurface cavities that extend from the Pratzim canyon system, possibly pointing to hydrologic links between the subaerial canyon system and a subsurface cave system. The 172 m long Flour Cave is the longest known cave in the area (Figure 2c). The cave has two openings; the lower which is located at the level of the Pratzim Canyon bed and the upper, which is a sinkhole, located approximately 150 m to the southeast. It is worth noting that the cave was famous as a tourist attraction, but since 2005 it was closed to the public due to frequent rock collapse within the cave and close to its upper opening.

3 Methods

3.1 Mapping geomorphic landforms

Geomorphic mapping was carried out based on field surveys and analysis of orthophotos and a high resolution (0.5 m/pixel) DEM. The DEM was generated from airborne LiDAR data with ground sampling resolution of 4 pts/m^2, sub-meter georeferencing, and vertical accuracy and precision of 0.15 m and 0.05 m, respectively. Based on the orthophotos, DEM, and a derived slope map, we manually delineated the cliff edges of the Pratzim canyon system, and identified and mapped the boundaries (edges) of sinkholes and courtyards, and the trace of surface lineaments (Figure 3). These geomorphic landforms are defined herein as follows: Sinkholes are deep depressions, completely surrounded by the intact strata of the Lisan formation at the topographic level of Ami'az Plain. Sinkholes do not have a subaerial hydraulic connection with the drainage system. Courtyards are morphological depressions partly surrounded by intact strata of the Lisan formation at the level of Ami'az Plain and partially connected to the Pratzim canyon system. Courtyards commonly appear as semicircular to elongated local extensions of the canyon system, and they are mapped as part of the canyon system polygon. Surface lineaments are long, narrow, shallow to intermediate depressions (with a depth range of several tens of centimeters up to a few meters) on the surface of Ami'az Plain. Cliff edges, sinkholes, and courtyards were mapped as polygon layers, whereas the lineaments were mapped as polylines. Figure 3 shows examples of sinkholes (purple), courtyards (red) and lineaments (green) mapped over an orthophoto and a slope map.

To associate the mapped sinkholes, courtyards, and lineaments with the Pratzim drainage network, we extracted flow pathways based on a D8 flow routing algorithm after filling local sinks. The drainage network was defined by using a drainage area threshold of 10,000 pixels (2500 m^2) and an elevation threshold < -268 m bsl. To discard flow pathways that flow at the level of Ami'az Plain, we accounted only for pixels that are contained within the canyon system polygon.

3.2 Morphometric measurements

To evaluate the eroded volume from the canyon system, we generated an interpolated high-order polynomial surface across Ami'az Plain after removing the pixels contained within the canyon system and sinkholes polygons. The eroded volume was calculated by subtracting the interpolated surface from the DEM at the pixels of the canyon system and multiplying by the pixel area.

A density map of the sinkholes and courtyards was generated using ArcGIS non-weighted kernel density algorithm with a search radius of 100 m and an area unit of 1 km^2. The density map was based on a layer of points that represent the centroids of each sinkhole and courtyard and is independent of the feature area.

To define tributary orientation, junction branching angles (Seybold et al., 2017), and channel bend angles, the drainage network pixels were divided into segments. Each segment was defined such that it is bounded at both ends by a channel head, a junction or a bend pixel (bends were located manually). The pixels between segment bounds are not junctions or bends. Segments that originate at a channel head pixel and are shorter than 50 pixels are omitted from the analysis. The orientation of each channel segment was defined as the

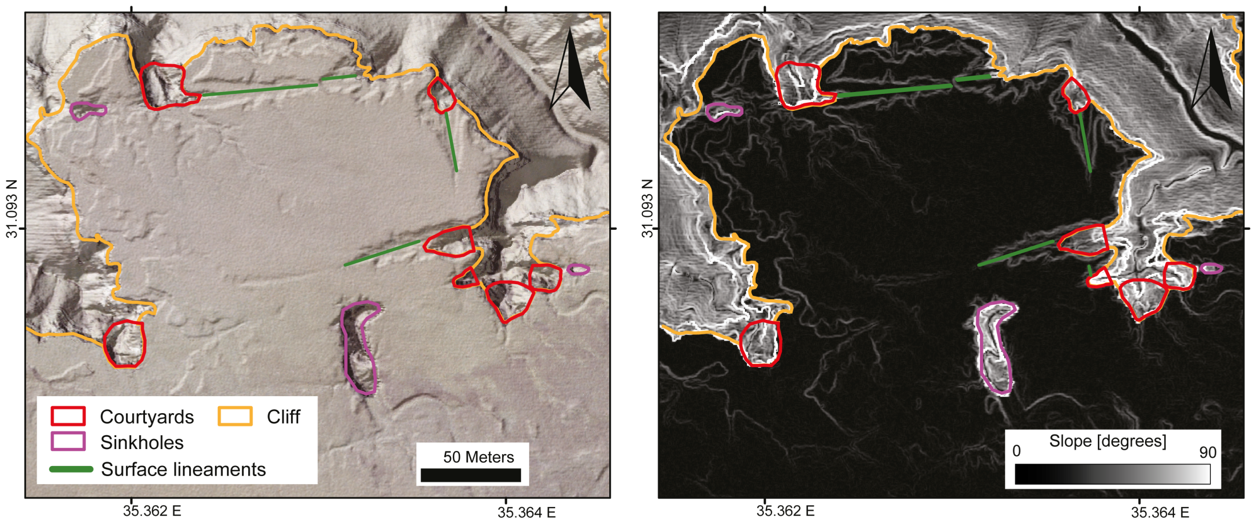

Figure 3: Examples of geomorphic landforms in the Ami'az Plain: cliff (orange), courtyards (red), sinkholes (purple) and surface lineaments (green). A shaded relief map combined with an orthophoto (left) and a slope map derived from a 0.5 m/pixel DEM (right) were used to identify and delineate the landforms.

northern hemisphere bearing of an orthogonal linear regression through the pixels of the segment. The junction branching angles were defined as the angle between the two segments that drain to the junction (Seybold et al., 2017). Bend angles were defined as the smaller angle that forms between the two segments that share a bend pixel. Intersection angles between cross-cutting lineaments were defined as the acute angles.

3.3 Ground-based LiDAR scanning

The Flour Cave is located in the center of the study area, at 31.084757° N 35.356255° E (Figure 2c). To map the 3D interior structure of the Flour Cave and its entrances we used a tripod-mounted Leica BLK360 laser scanner. A total of ∼320 million data points were collected from 19 sub-scans to map the cave interior at ∼5 cm spacing and at cm-scale accuracy.

3.4 Field-based internal erosion experiments

To examine the susceptibility of the infilled material of the clastic dikes to internal erosion and the associated morphological changes, we conducted three field experiments. The experiments were executed in a unique location, where a 4.5 m wide surface lineament exposes at its base a 0.18 m wide clastic dike, seen also at the perpendicular cliff face (Figure 4). The lineament drains an area of 2600 m^2 to a narrow notch along a canyon bank. The upper part of the dike intrudes through a 0.5 – 1 m of the upper member of the Lisan formation consisting of alternating gypsum and thin marl horizons.

The first experiment consisted of a preparation stage (Feb. 6, 2019), two subsequent natural rain storms of 11 and 1 mm rain depth that occurred on Feb. 7 and Feb 18, respectively, and post-storm documentation conducted on Feb. 20, 2019. During the preparation stage, we exposed the clastic dike and the gypsum layer bounding it by removing a thin layer of overlying fine deposits. We excavated a half ellipse-shaped depression (referred to herein as the 'experimental pool') into the dike. The long axis of the ellipse was 25 cm, the depth of the pool was 5 cm, and the width of the pool, set by the width of the clastic dike was 18 cm. The center of the experimental pool was 47.5 cm from the cliff. The post-storm documentation revealed indications of overland flow in the form of muddy channel beds along the Pratzim Wadi and in the experimental site. Field measurements were conducted to record morphological changes in the experimental pool and along the cliff, where the clastic dike is exposed.

The second and third experiments were conducted consecutively on February 20, 2019, by manually filling the experimental pool. For these experiments, the long axis and the depth of the experimental pool were extended to 86 cm and 20 cm, respectively. At the beginning of the second experiment (hereafter, 'water-level drop' experiment), the pool was filled to where the maximum water level was set to 11.5 cm above the deepest point of the pool. We then simultaneously recorded the rate of water level drop in the experimental pool and water seepage from the clastic dike exposure on the cliff (Figure 4c).

In the third experiment, (hereafter, 'constant water-level' experiment), we maintained a constant water level of 12 cm for 8.5 min and then 19 cm for additional 18 min, while documenting water seepage from the clastic dike exposure along the cliff, and morphological changes at the surface. Water level was maintained by adding water whenever the water level at the experimental pool dropped by 1 cm.

4 Results

4.1 Drainage network and geomorphic landforms

4.1.1 The Pratzim canyon system

Based on the field surveys and geomorphic mapping, we divide the study area into two distinct regions (Figure 5a). Along a relatively narrow N-S trending strip in the west part of the study area (hereafter, 'western region') the channel system exhibits a predominately dendritic pattern (see also junction branching angels in section 4.3). The canyon cliffs follow the course of the meandering channels at the base of the canyons, and the channels gradually incise from the level of the Ami'az Plain forming linear long profiles (Figure 5b). Valley cross sections exhibit, in most cases, sloping banks with 'V' to 'U' canyon-shaped morphologies (Figure 5e).

Along the central and eastern parts of the study area (hereafter, 'central region'), the channel system froms a predominately rectangular drainage pattern (see also junction branching angels in section 4.3). Each individual tributary maintains an approximately constant width that ranges from several meters and up to 170 m, and the course of the bounding cliffs is linear in plan-view, i.e., non-meandering. The canyon valleys reach depths of up to 35 m, and the upper section of the banks is typically sub-vertical.

The canyons in the central region terminate abruptly in steeply plunging vertical channel heads (Figure 5c) with variable planform morphology, ranging from sub-circular (i.e. amphitheater headed valley) (Figure 6a) to sub-rectangular and irregular. The vertical channel heads are fed by shallow channels that traverse the Ami'az Plane. Notably, in some cases,

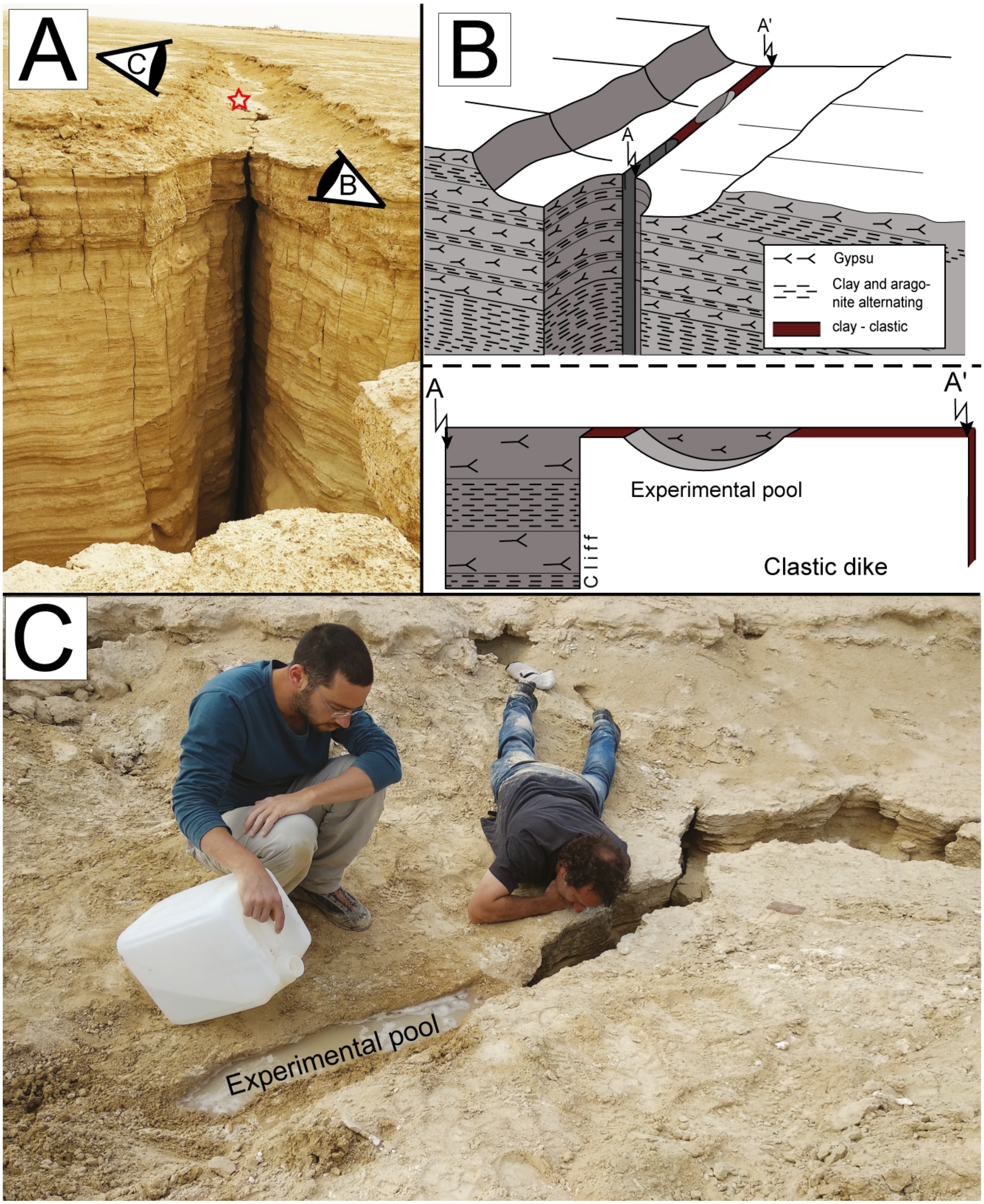

Figure 4: (a) The experiment site showing the surface lineament draining an area of 2600 m^2 to the cliff. The red star marks the location of the experimental pool. Its coordinates are 31.0844 N, 35.3630 E. The 'eye' symbols represent the view direction of panels b and c. The width of the lineament at the cliff is 4.5 m. (b) Schematics of the geometry of the experiment site with the Lisan formation. Cross section A – A' shows the geometry parallel to the lineament. (c) Photo of the third field experiment showing the ponding water and documenting flow out of the cliff. The location of the experiment site is marked in figure 5a.

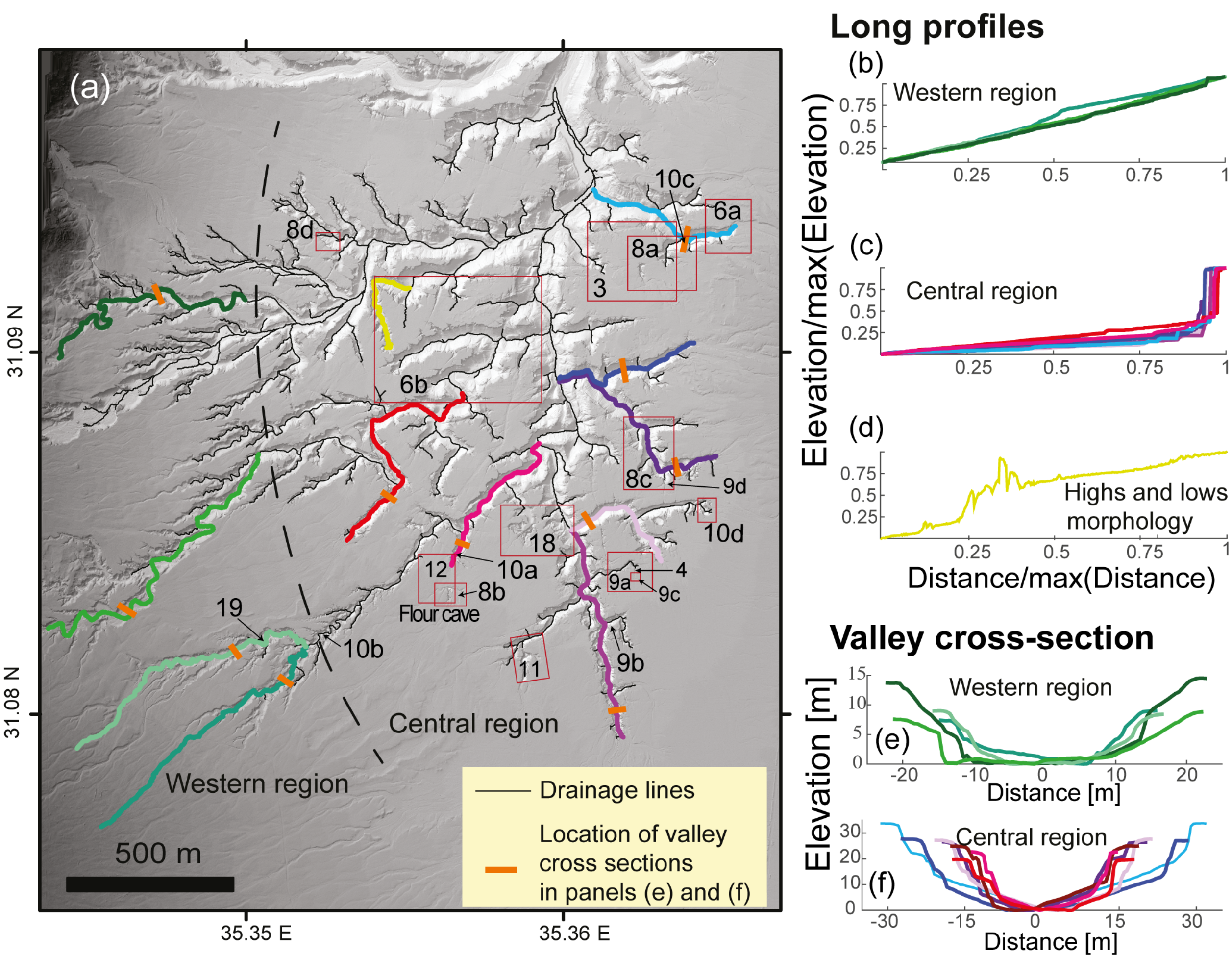

Figure 5: (a) Shaded relief map of the Pratzim channel network in Ami'az Plain based on a 0.5 m/pixel DEM. The thick black dashed curve marks the boundary between the western and the central regions. The drainage network is depicted by thin black lines. Numbered arrows and rectangles refer to locations of maps and photos in following figures. Colored channels refer to panels (b) – (f). (b,c) Normalized longitudinal profiles of channel segments in the western and central regions, respectively. (d) Longitudinal profile of a channel with highs and lows morphology due to accumulation of collapsed bank material. In this tributary, drainage occurs partly at the subsurface as shown in figure 10c for a different tributary. (e,f) Valley cross sections of selected tributaries in the western and central regions, respectively.

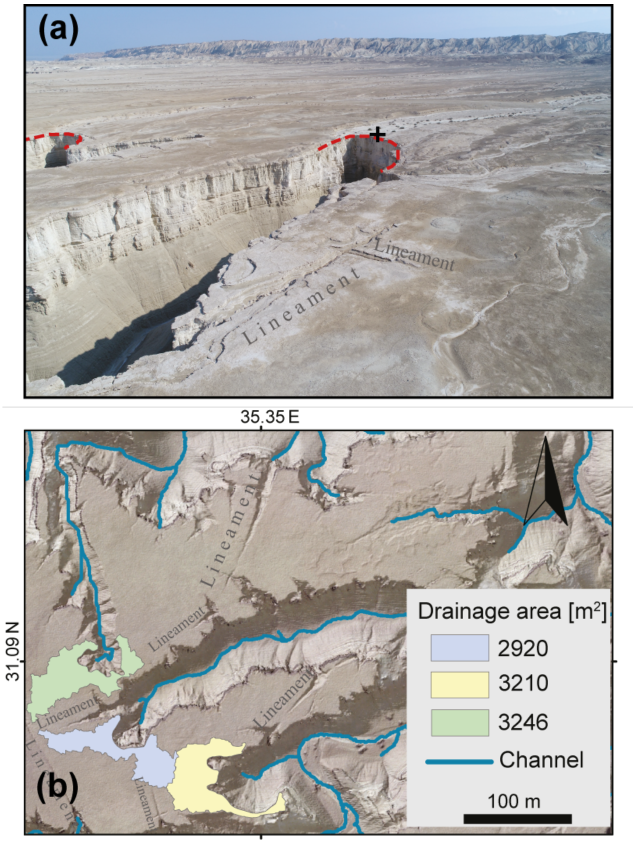

Figure 6: (a) A photo of two amphitheater channel heads. Dashed lines mark the edge of the canyon cliff at the heads. The diameter of the right amphitheater is 25 m. The coordinates of the black + symbol are 31.0937 N, 35.3662 E (b) Examples for three steep channel heads with exceptionally small drainage areas.

feeding channels are missing and the drainage area at the channel head is only several thousands of m^2 (Figure 6b). Along the wider canyons, the channel bed is relatively flat, and it dips downriver with an approximately constant shallow slope (Figure 5c). Colluvial aprons grade from the canyon banks to the flat river bed covering the lower parts of the banks (Figure 5f), and the active streams often meander between the canyon wall aprons. In other places, where canyons are narrow, collapsed bank material fully covers the river bed, creating morphological highs-and-lows that prohibits overland hydraulic connectivity (Figure 5d).

4.1.2 Sinkholes and courtyards

Mapping of geomorphic landforms revealed 141 sinkholes that are predominantly located in the central region (96% of the sinkholes), in close proximity to the canyon system (Figure 7a). The area of individual sinkholes ranges between 1 and 1650 m^2 (average of 90 m^2 and standard deviation of 260 m^2), and their morphology varies between circular, to rectangular, elongated, and amorphous (Figure 8a and 8b). Sinkhole depths range between $\sim$1 to 24 m. In most cases, where access or view was possible, a subsurface hydraulic connection was verified between sinkholes and the adjacent canyon system through narrow elongated caves.

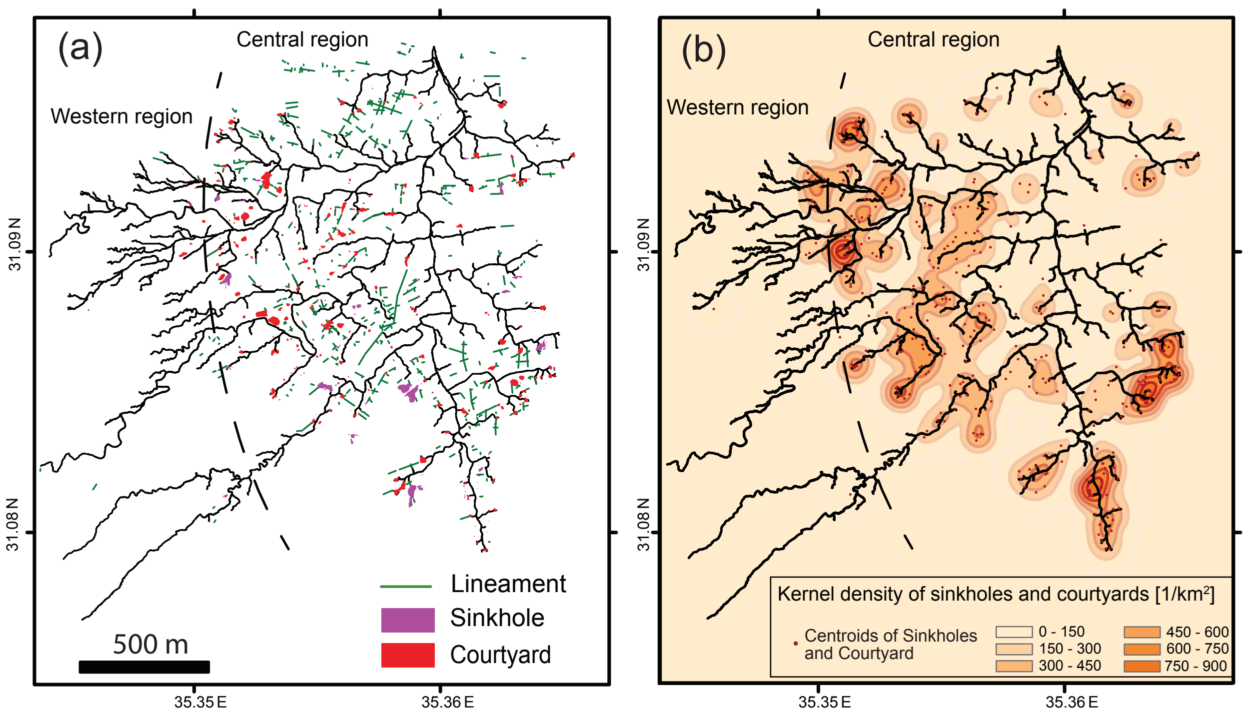

Figure 7: (a) Map of sinkholes (purple), courtyards (red) and surface lineaments (green) in the study area overlain on the flow lines of the Pratzim drainage network. (b) Kernel density map of sinkholes and courtyards superimposed upon the Pratzim drainage network. Dashed curves mark the boundary between the central and western regions

We mapped 212 courtyards that, like sinkholes, are predominantly located in the central region (95% of the courtyards). The area of individual courtyards ranges between 5 to 1122 m^2 (average of 157 m^2 and standard deviation of 187 m^2), and their shape is characterized by a sub-circular to elongated morphology (Figure 7a, 8c and d). In some cases, the collapsed material bounds the courtyard and prohibits subaerial hydraulic connectivity to the canyon system (Figure 8d). In other cases, the courtyards are fully connected to the canyon and appear as an extension of the canyon. Numerous canyon tributaries show clusters of courtyards that effectively widen the canyon (Figure 8c) .

Figure 7b reveals that the distribution of sinkholes and courtyards in the study area is not uniform. Regions of high sinkhole/courtyard density occur mostly at the upper bounding edge of the canyon system in the central region and particularly near channel heads. A somewhat lower density is found near the main channel of the Pratzim canyon system in the central region. Courtyards and sinkholes are almost absent in the western region.

En echelon joints are commonly seen parallel to the banks of the canyon system, courtyards, and sinkholes (Figure 8b). In numerous cases, the joints are deep and they fully bound blocks that recline against the walls of the canyons and sinkholes. Some of these blocks slide down or rotated, effectively widening the canyons and sinkholes.

4.1.3 Surface lineaments

We mapped 434 surface lineaments in the study area, with $\sim$ 98% of the lineaments occurring in the central region (Figure 7a). Lineament lengths range between 2 and 137 m (average of 18 m and standard deviation of 17 m), and their width is up to 9 m. Some of the lineaments drain directly to the canyon system at channel heads, banks, and courtyards (Figure 9a, 9b, and 9d) and in some cases, lineaments terminate at a narrow land bridge that separates the lineament from the canyon (Figure 9a). Other surface lineaments drain into sinkholes, and in few cases, both ends of the lineament terminate within Ami'az Plain, and they appear to lack surface drainage (Figure 9a). We also observed that surface lineaments commonly cross each other at right angles (Figure 9a, 9c and 9d).

4.1.4 Caves

Cave openings are abundant along canyon banks and heads in the central region, and they appear at variable elevations, from the top of the canyon banks (Figure 10a) and downwards to the base of the canyons (Figure 10b and 10d). Cave opening diameter ranges between tens of cm to several meters. In places where narrow tributaries are blocked by collapsed bank material, caves cut under topographic highs formed by the collapsed material and open subsurface hydraulic routes (Figure 10c).

We surveyed several caves that extend from the canyon system in the central region. Caves are typically elongated and narrow, and are characterized by variable cross-section geometry, including rectangular with vertical side walls, elliptical, and keyhole-like shape with circular or elliptical upper end that connects to a rectangular lower end. Along some of the caves, we documented large halls with arc-like or flat ceiling that forms along distinct bedding plains exposed by collapsed blocks. The deposits of the collapsed ceiling can sometimes be identified on the cave floor, and secondary caves often cut through the collapsed deposits. When a section of the cave ceiling is completely missing, this section becomes a sinkhole that

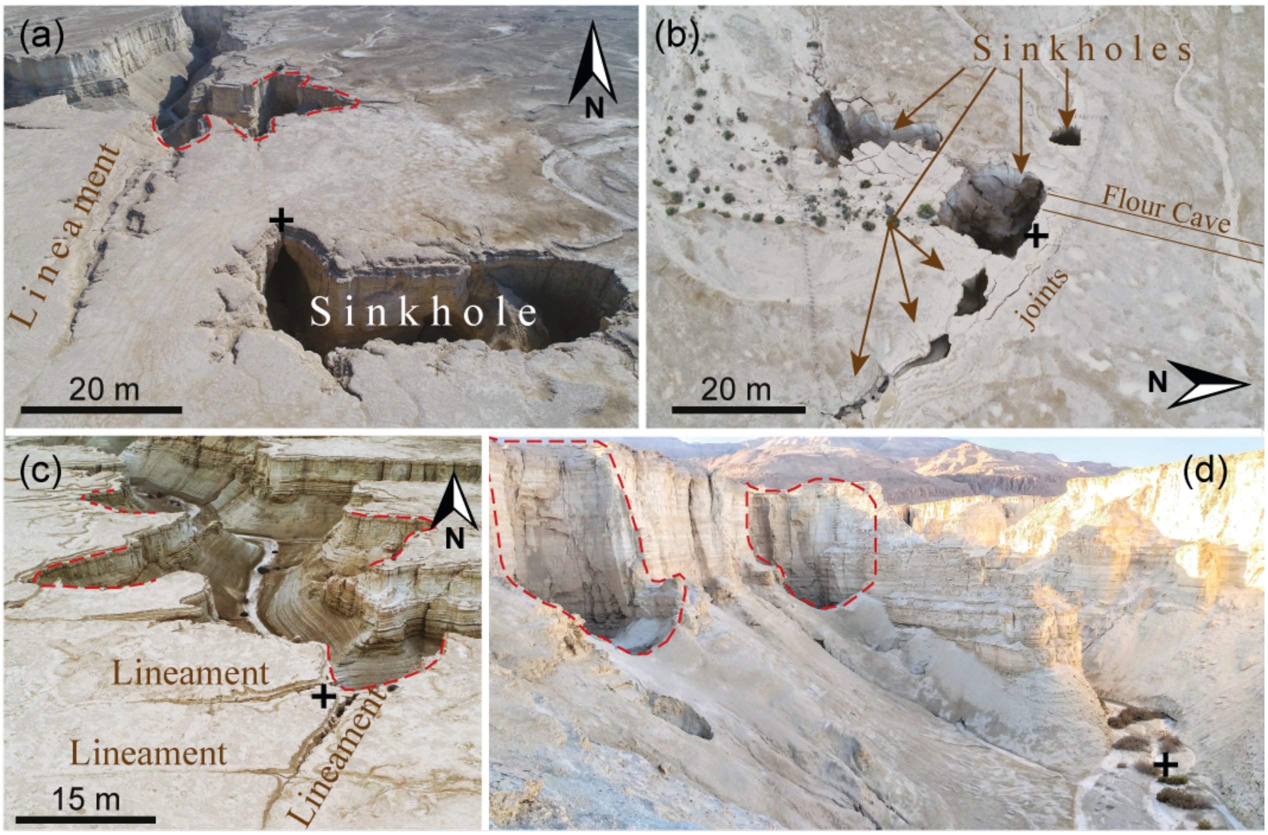

Figure 8: (a) Drone photo of a large, elongated sinkhole. Note the nearby lineaments that are connected with the courtyard (marked by red dashed curves). The coordinates of the black + symbol are 31.0927 N, 35.3634 E. (b) Drone photo of a series of sinkholes at the upper entrance to the Flour Cave. Note the joints parallel to the sinkhole edges and the vegetation that marks surface drainage into the sinkholes. Black + symbol coordinates: 31.0839 N, 35.3571 E. (c) Drone photo of a canyon tributary with four distinct courtyards, marked by red dashed curves, effectively widening the tributary. Black + symbol coordinates: 31.0867 N, 35.3639 E. (d) View of two courtyards (marked by red dashed polygons) from the level of a canyon tributary. The height of the steep vertical cliff at the foreground is 7 m. Black + symbol coordinates: 31.0935 N, 35.3534 E.

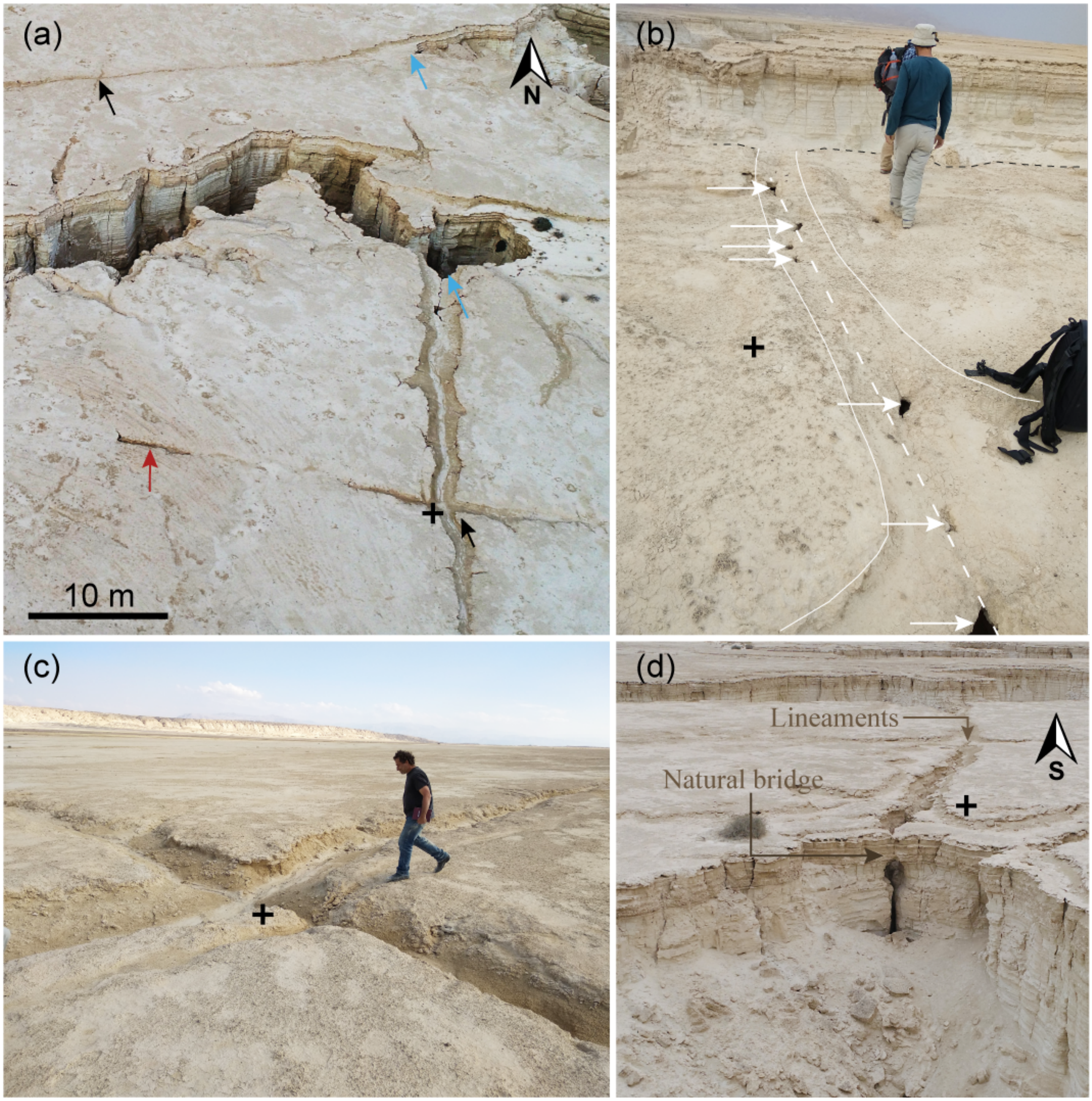

Figure 9: (a) Drone photo of deep and narrow canyon tributaries with nearby surface lineaments. Black arrows point to cross-cutting lineaments with an approximately right angle, red arrow points to a short lineaments with no surface drainage, and light blue arrows point to lineament outlets at courtyards. The proximal blue arrow is located at our experiment site. Black + symbol coordinates are 31.0841 N, 35.3630 E. (b) A linear series of small holes (white arrows), interpreted as an embryonic lineament. The white lines boarder a subdued surface depression that accompanies the holes. Dashed black line marks cliff edge. Black + symbol coordinates are 31.0828 N, 35.3623 E. (c) Close-up view of right-angle cross-cutting lineaments. Black + symbol coordinates are 31.0841 N, 35.3630 E. (d) A lineament draining toward a canyon cliff under a narrow rock bridge. Right-angle cross-cutting lineaments at the background. The height of the steep section of the cliff is 4 m. Black + symbol coordinates are 31.0867 N, 35.3639 E.

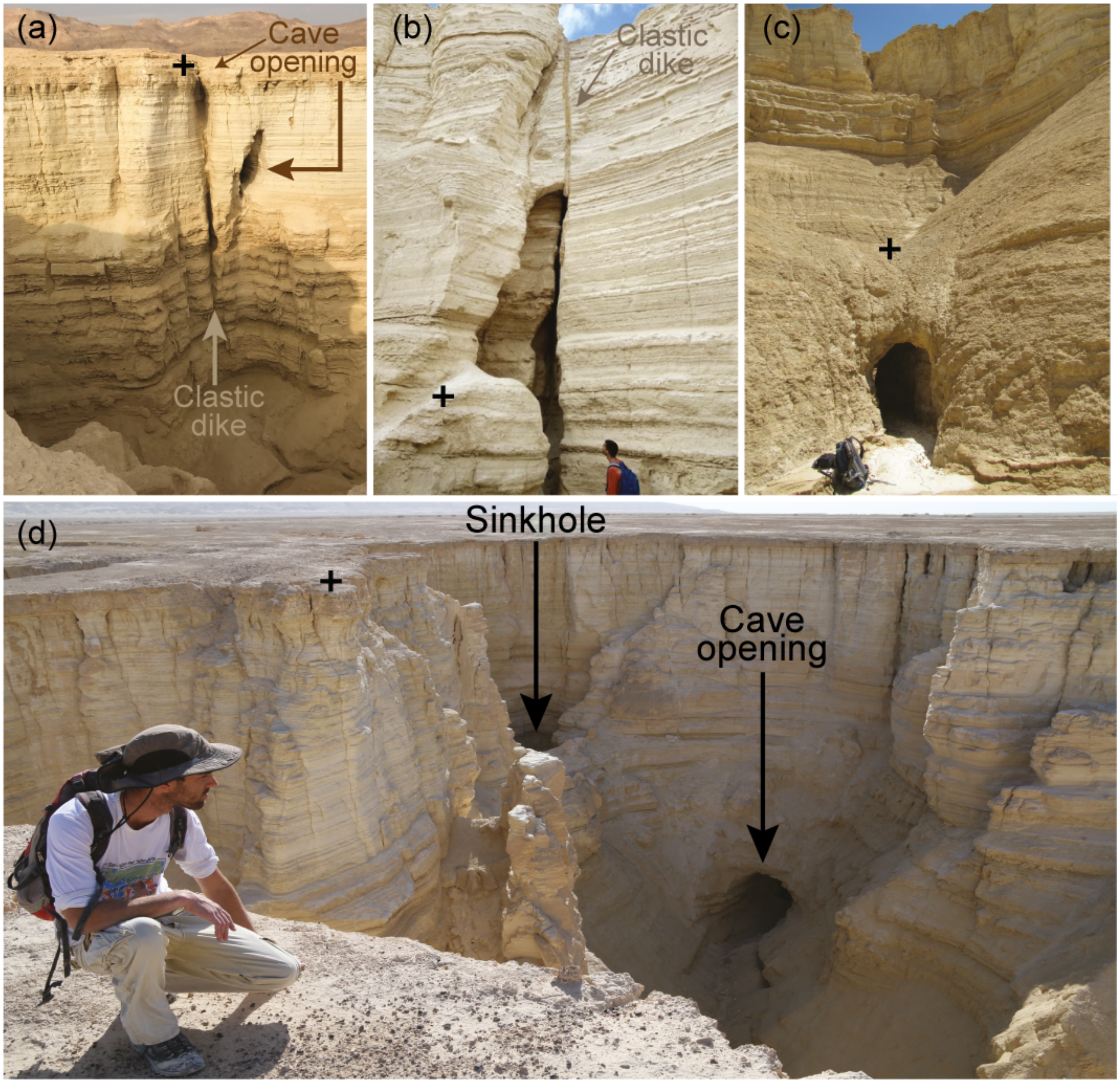

Figure 10: (a) Caves opening along a canyon tributary bank. The top opening is along a clastic dike, and the lower opening is close to the dike. Canyon bank is 20 m high. Black + symbol coordinates are 31.0850 N, 35.3571 E. (b) A cave opening to the side of a clastic dike extending from the base of the channel. Black + symbol coordinates are 31.0827 N, 35.3530 E. (c) A cave within collapsed bank material. A backpack for scale. Black + symbol coordinates are 31.0933 N, 35.3644 E. (d) A cave opening at the base of a channel head, and a sinkhole beyond the channel head. The cave opening diameter is ∼2 m. Black + symbol coordinates are 31.0861 N, 35.3652 E.

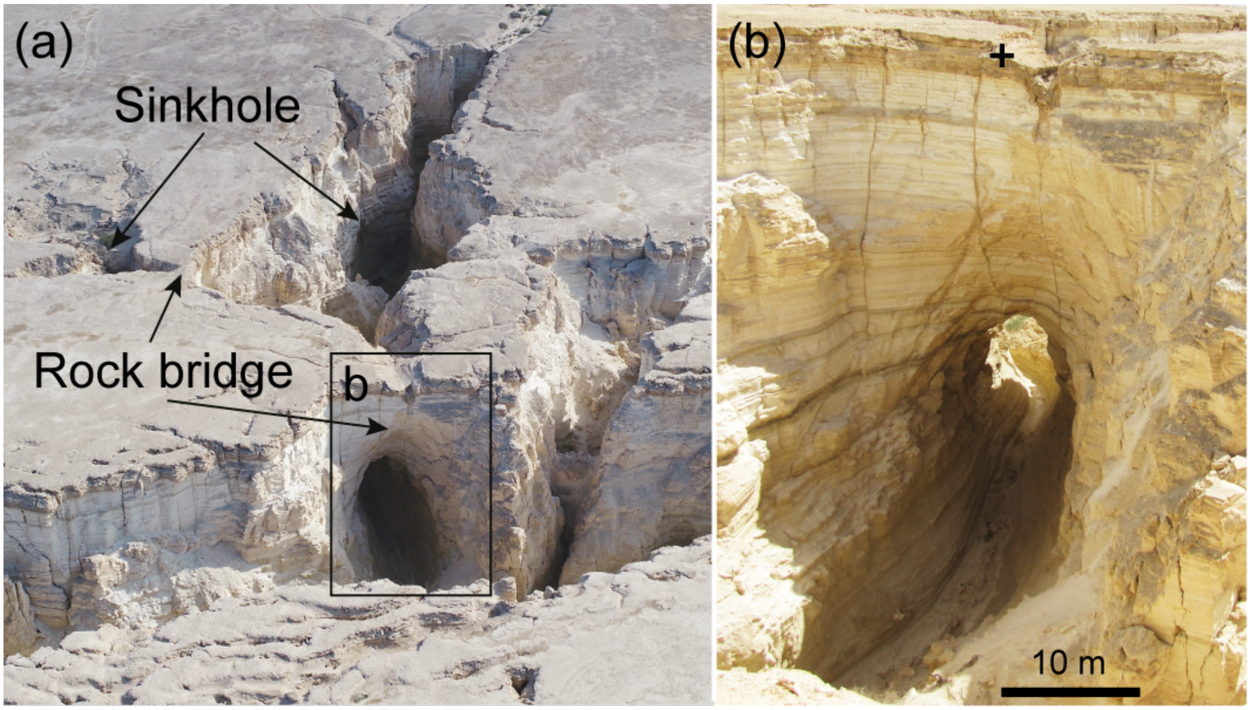

Figure 11: (a) Drone photo of two rock bridges. The bridge in the foreground separates between an elongated sinkhole and a tributary of the Pratzim network. The bridge at the left of the image separates two neighboring sinkholes. Solid rectangle marks the view of panel (b). (b) Close-up on the foreground bridge from (a). Note the fluvial-like pathway under the bridge and the two clastic dikes that dissect the bridge. Black + symbol coordinates are 31.0822 N, 35.3595 E.

connects hydraulically to the canyon system through the cave. When two sinkholes form next to each other, or when a sinkhole is located close to the cave opening along the canyon bank, the cave ceiling becomes a local rock 'bridge' (Figure 11).

The ground LiDAR scanning of the Flour Cave covered a length of 145 m from the lower cave's opening (outlet) along the Pratzim canyon bank up to the upper cave's opening, a sinkhole in Ami'az Plain (Figures 8b and 12). The width of the cave varies between 0.95 and 5.5 m, and the cave height above its floor ranges between 3.2 and 12.8 m, with an estimated average of 6 m. The thickness of the Lisan rocks above the cave ranges between 5 and 14.7 m. The cross section of the cave varies between a keyhole-like morphology (Figure 12b, d, and e) to a narrow and elongated shape with vertical walls (Figure 12c). Two high and wide halls and a chimney that extends upward and reaches 7.7 m below the surface of Ami'az Plain were documented (Figure 12d and e) . Along most of the cave, clastic dikes are exposed at the celling, parallel to the cave course (Figure 12b-e). Intersecting clastic dikes were observed in places where the cave's ceiling is relatively high, including in both halls (Figure 12d and 12e). Collapsed bank and ceiling material appears as terraces at the floor of the cave, mostly within the halls.

A courtyard was mapped immediately at the outlet of the Flour Cave. Two perpendicular clastic dikes are exposed at the walls of this courtyard, parallel and perpendicular to the direction of the lower section of the cave. The Flour Cave is experiencing ongoing collapses and morphological changes. Until at least mid 2004, there was a narrow land bridge above the flow path between the courtyard and the canyon tributary into which the Flour Cave drains, making this courtyard a former sinkhole.

4.1.5 Clastic dikes

Field observations in the central region revealed spatial relationships between the clastic dikes and the mapped geomorphic landforms of caves, sinkholes, courtyards, surface lineaments, and canyon walls. Almost all the channel heads we surveyed had at least one clastic dike exposed in them. In several cases, canyon walls are nade of a clastic dike plane, whose infilling material was mostly eroded. Cave openings typically appear along or close to clastic dikes (Figure 10a and 10b), and clastic dikes are commonly exposed at the cave ceilings (Figure 12b-e). Clastic dikes also crosscut the walls of sinkholes and courtyard, and they bind narrow rock bridges (Figure 11). In the experiment site, a clastic dike was exposed at the base of the lineament, and in other outcrops, where lineaments drain to the canyon, clastic dikes were observed directly beneath lineament outlet (Figure 9e), in agreement with Jacoby et al. (2015), who mapped the lineaments as morphological expressions of dikes.

4.2 Erosion rate

The volume of the eroded material from the Pratzim canyon system is 16.8×10^6 m^3. Dividing the eroded volume by the area of the canyon system polygon, we obtained an average erosion depth of 16.9 m. Because clastic dike emplacement likely predates canyon formation in the Ami'az Plain, we use the clastic dikes emplacement ages from Porat et al. (2007) as an upper bound for the onset of erosion. Dividing the average erosion depth by the age of the youngest dike of 10.1 ± 0.9 Ka (Porat et al., 2007) yields a minimum average erosion rate of 1.54-1.84 mm/yr.

4.3 Drainage pattern and orientation

Figure 13a depicts the length-weighted orientation histogram of channel segments, such that longer segments are more heavily represented. Three dominant peaks appear. The east-northeast (ENE) orientation is the most dominated, and the two other peaks are to the north-northwest (NNW) and to the west (W). Although these peaks are well-recognized, river segments populate all other orientations in between the peaks. Figure 13b shows a length-weighted orientation histogram of the surface lineaments in the study area. The histogram is characterized by three dominant peaks: ENE, N, and W.

Figure 14a shows the distribution of junction branching angles and stream bends of the Pratzim canyon system. In the western region, the branching angles show a skewed distributed with a greater representation of low, 10°-40° angles. Bend angles in this region range between higher values of 70°-150° (Figure 14c). In the central region, angles appear to distribute more normally with a modal value around 90°. Here as well, bends tend to have greater angles than junctions (Figure 14d). We note that the branching angle analysis is conservative in the sense that we estimate only one angle per junction, the angle between the two segmentes that drain toward the junction. There are many cases where the angle between one of these segments and the channel segment immediately downstream from the junction is significantly

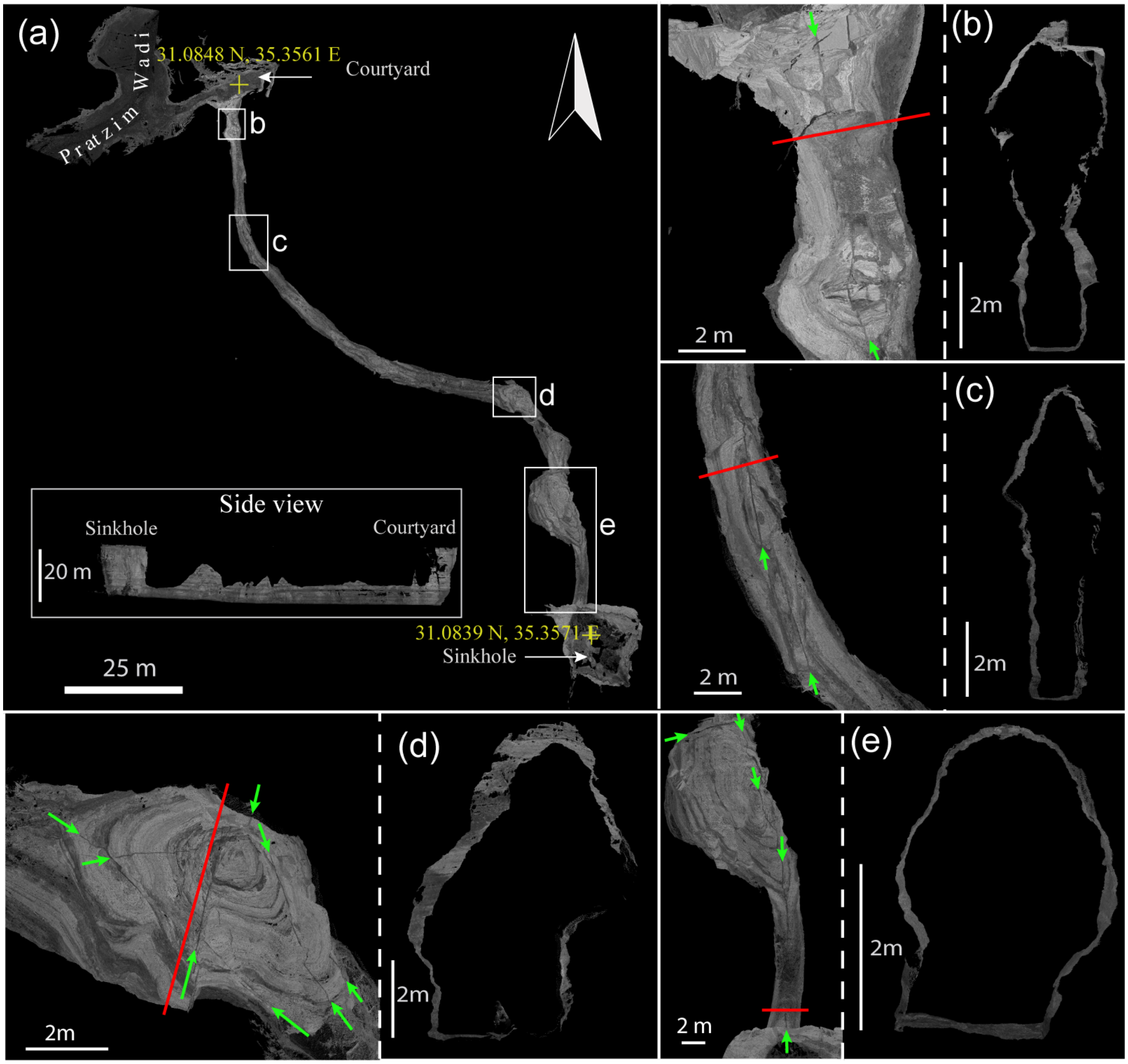

Figure 12: Merged point clouds and cross sections along the Flour Cave. Grayscale represents intensity values. (a) Map view of the Flour Cave route. White rectangles refer to panels (b)-(e). The inset shows a side projection of the Flour Cave. Red coordinate marks are in the Israel Transverse Mercator. (b)-(e) Close-up of specific locations along the cave. The left side of each panel shows the ceiling, where green arrows point to clastic dikes identified based on intensity contrast with the laminated Lisan rocks. The right side of each panel shows the cave cross-section along red lines.

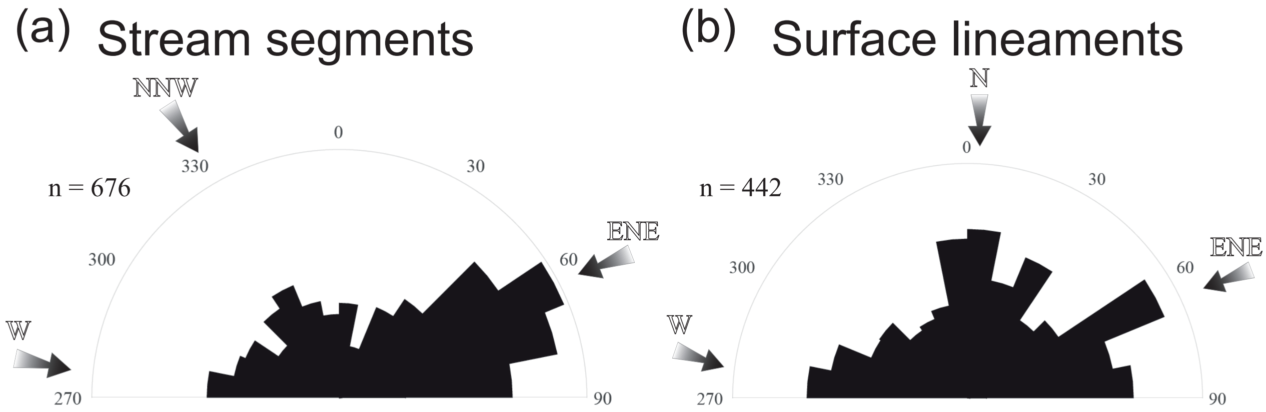

Figure 13: Length-weighted rose diagrams of stream orientation (a) and surface lineaments (b).

closer to 90°. Despite this conservative choice, the current quantitative analysis corroborates the rectangularity of the Pratzim canyon system in our study area (Figure 14a and b).

Figure 15 shows an histogram of angles for intersecting surface lineaments. The analysis shows that $\sim$72% of the angles are $> 75°$ and 41% of the angles are $> 85°$. These measurements indicate that most of the intersecting surface lineaments are sub-orthogonal to orthogonal.

4.4 Field experiments of internal erosion in clastic dikes

The abundant caves in the study area are interpreted as pipe caves formed by internal erosion (see discussion in section 5). Motivated by the spatial association between clastic dikes and caves, we designed the field experiments to explore the feasibility of internal erosion and pipe formation within the material that infills clastic dikes. The first field experiment was based on natural rain storms. Following the storms, we observed the formation of an alcove that extended 25-30 cm from the vertical cliff inward and toward the experimental pool. The alcove opening at the cliff face formed approximately 18 cm below the surface, and it was closed at its far end, i.e., no macro pipe was observed.

In the second, 'water-level drop' experiment, we measured a continuous water level lowering. The water level - time data shows an exponential decay relation with a timescale of 2000 s (Figure 16a). Flow out of the alcove and down the cliff was first documented 153 s from the onset of the experiment, when the water level was at 10 cm above the base of the pool, (i.e. after a drop of 1.5 cm in water level). The flow continued intermittently (as pulses of flow followed by no flow periods) for 725 s, until the water level dropped to 7 cm above the base. From this stage and until the end of the experiment, no flow out of the alcove was observed while the water level in the excavated experimental pool continued to drop (see also Table A1 in Appendix A). The water expelled out from the cliff during the experiment was muddy, and we observed several collapse events of the alcove walls. At the end of the experiment, the alcove was extended in the direction of the experimental pool, but still, no macro-scale pipe was formed.

To explain the excellent exponential fit to the trend of water level drop in the second experiment, we developed an idealized theoretical model of porous flow in between the ex-

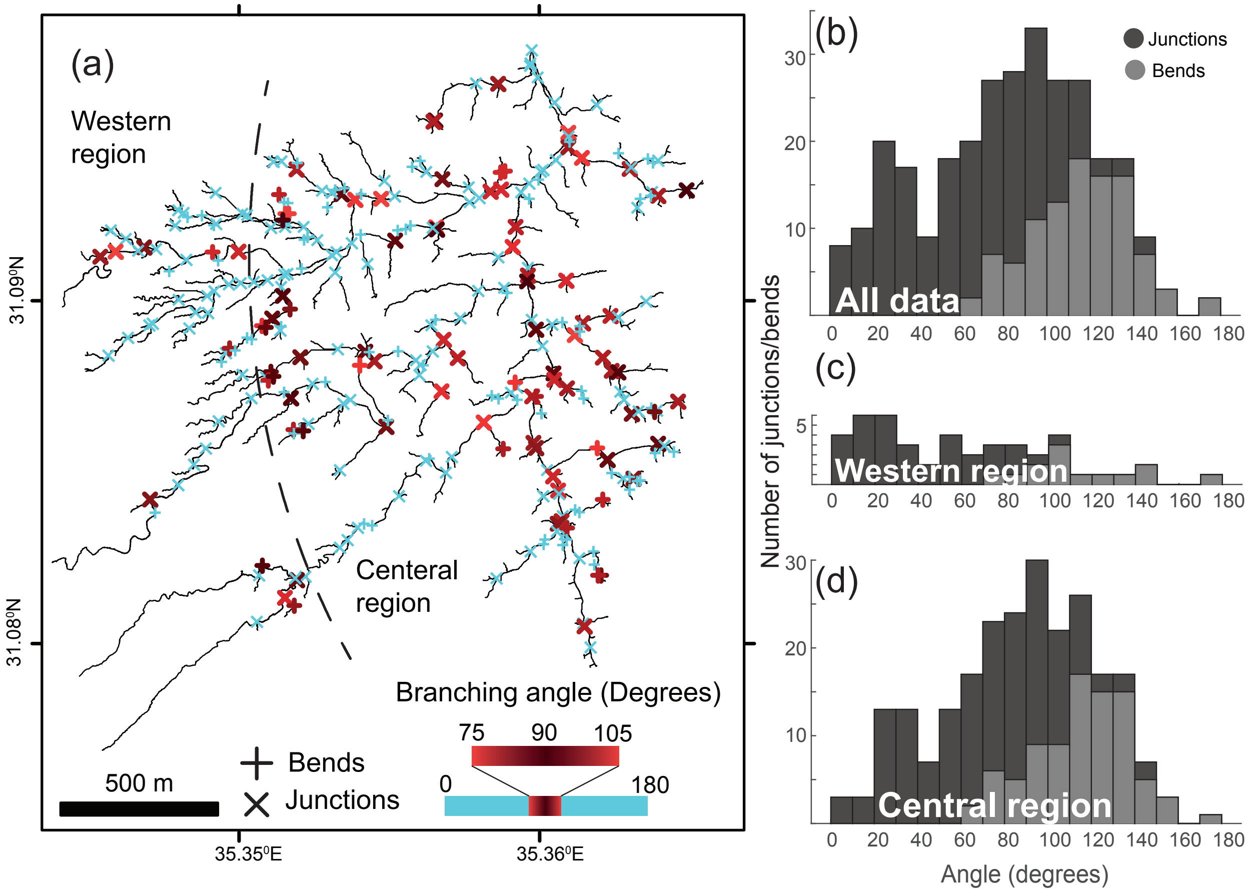

Figure 14: (a) Junction branching angles (x) and stream bend angles (+) shown on a map of the Pratzim drainage network. Red colors are for the angle range of 75-105°, typical of rectangular drainages. Light blue color is used for smaller or larger angles. Note that our definition for the range of rectangular angles does not overlap with the dominant branching angle of 72° found across humid regions that are dominated by groundwater-fed streams (Devauchelle et al., 2012; Seybold et al., 2017). (b) - (d) Histograms of junction branching angles (dark gray) and stream bend angles (light gray). (b) Whole region. Junctions: [number, median, std]=[193,68.4°,33.3°]. Bends: [number, median, std]=[101,115.0°,23.2°]. All points: [number, median, std]=[294,86.7°,38.2°]. (c) Western region. Junctions: [number, median, std]=[41,33.5°,28.2°]. Bends: [number, median, std]=[14,108.0°,27.4°]. All points: [number, median, std]=[55,52.7°,42.6°]. (d) Central region. Junctions: [number, median, std]=[152,75.5°,31.5°]. Bends: [number, median, std]=[87,116.0°,22.7°]. All points: [number, median, std]=[239,90.8°,35.2°].

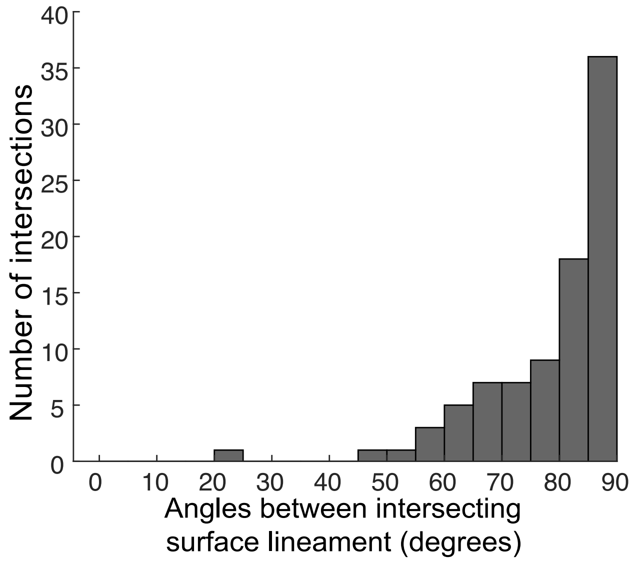

Figure 15: Histogram of the acute cross-cutting angles of intersecting surface lineaments.

perimental pool and the cliff. The model relies on a simplified two-dimensional rectangular geometry of the experimental setting (Figure 16b), and on an assumption of a one-dimensional Darcian porous flow:

$$\Phi U_f = -\frac{k}{\eta}\frac{dP}{dx}, \tag{1}$$

where Φ represents the porosity of the dike filling material, U_f is the water velocity within the porous media [m/s], k is the permeability of the clastic dike infilling material [m^2], $\eta = 10^{-3}$ Pa s is the viscosity of water, and dP/dx [Pa/m] is the horizontal pressure gradient between the experimental pool and the cliff. Along the cliff, the pressure is atmospheric, taken here to be zero, and the pressure at the base of the pool is $\rho_w g h(t)$, where $\rho_w = 1000$ kg/m^3 is the water density, $g = 9.81$ m/s^2 is the gravitational acceleration, and $h(t)$ [m] is the time dependent water level above the base of the pool. The pressure gradient can then be expressed as:

$$\frac{dP}{dx} = \frac{\rho_w g h(t)}{D_b}, \tag{2}$$

where $D_b = 0.12$ m is the shortest distance between the pool and the cliff (see Figure 16b). To evaluate $h(t)$ in equation (2), we incorporate a mass conservation consideration, stating that the flux of water that flows into the porous media and toward the cliff is balanced by water level drop in the pool:

$$\Phi U_f h_f = \frac{dh(t)}{dt} D_p, \tag{3}$$

where h_f [m] is the effective height above the pool base that accommodates porous flow, and $D_p = 0.86$ m is the length of the long edge of the pool. Combining equations (1) – (3) results in a differential equation for the water level within the pool, $h(t)$:

$$\frac{dh(t)}{dt} = -\frac{k}{\eta}\frac{\rho_w g h_f}{D_b D_p} h(t). \tag{4}$$

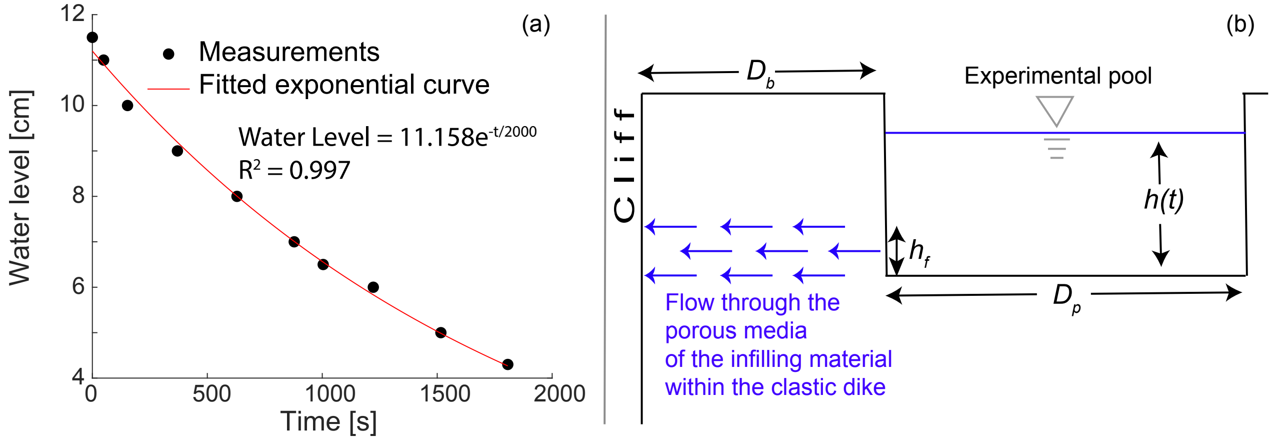

Figure 16: (a) Water level above the base of the experimental pool as function of time for the second 'water level drop' experiment. An exponential decaying trend excellently fits the measurements. (b) An idealized schematic model of flow through the porous media of the clastic dike's infilling material, developed to explain the observed exponential trend of water level drop.

The solution to equation (4) with the initial condition of $h(t=0)=h_0$ is:

$$h(t) = h_0 \exp\left(-\frac{t}{t_0}\right) = h_0 \exp\left(-\frac{k}{\eta}\frac{\rho_w g h_f}{D_b D_p} t\right). \tag{5}$$

The initial water level is $h_0 = 0.115$ m, and based on the exponential fit, we find that $t_0 = (\eta D_b D_p)/(k \rho_w g h_f) = 2000$ s. The only unknown parameters are h_f, the height of the porous flow, and k the permeability. Assuming that h_f ranges between 0.03 and 0.06 m allows us to estimate the effective permeability of the dike infilling material between the experimental pool and the cliff as 1.7×10^{-10} - 8.6×10^{-11} m^2. An independent measurement of the permeability of the dike's infilling material in a proximal location using a Mini Disc Infiltrometer device yielded approximately similar values of $1.1 \times 10^{-11} - 3.2 \times 10^{-12}$ m^2, supporting the inference that water level drop in the second experiment is associated with porous flow through the dike's infilling material toward the cliff.

In the third, 'constant water level' experiment, we observed flow out of the alcove that started 93 s after the onset of the experiment, when the water level was 12 cm above the experimental pool base. The expelled fluid was muddy, and the flow was nearly continuous with pulses of faster flow velocity (See Table A2 in Appendix A). During the experiment, two new flow outlets formed, one of them at the dike-wall boundary, and few collapse events of the alcove walls were observed. After 2037 s, we observed that the ground above the alcove began to subsided. Then, at 2080 s, a pipe was formed along the former trajectory of the alcove that fully connected the experimental pool to the cliff. Initially, the pipe opening had a sub-circular cross section with a diameter of 8.4 cm, and it rapidly (within few tens of seconds) drained the water above its opening. Rapid incision of the pipe base extended the pipe opening downward and formed a rectangular cross-section, overall generating a keyhole-like cross section (Figure 17).

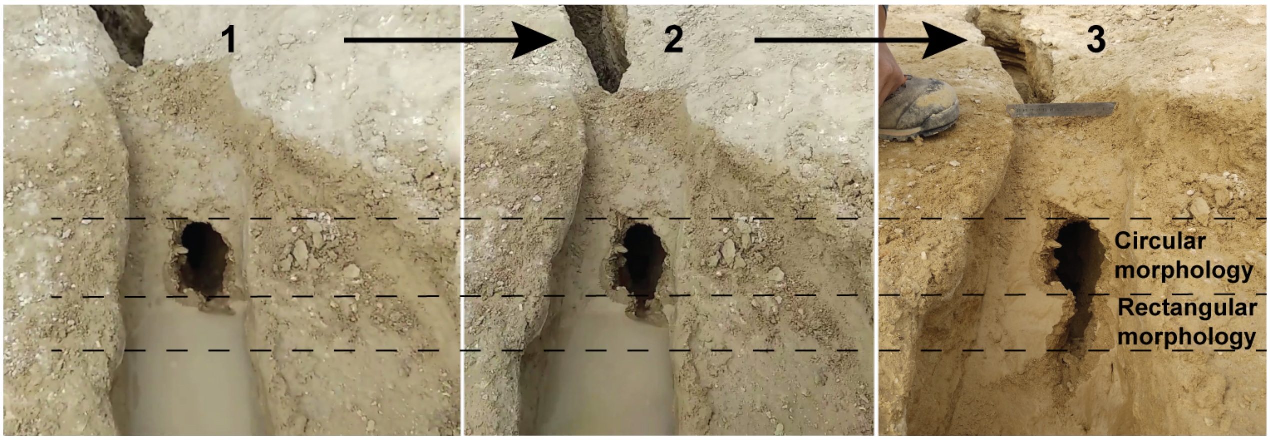

Figure 17: The inlet morphology of the pipe that formed at the end of the third, 'constant water level' experiment. The inlet has a keyhole-like shape, with a circular upper part and a rectangular lower part. Left: The upper, circular part was the first to form. Center: 29 seconds after the pipe formation, drainage of the remaining water in the experimental pool induced incision at the base of the pipe, extending the base of the inlet. Right: The inlet morphology after complete drainage of the water from the experimental pool, showing a developed key-hole like morphology. A 15-cm metal ruler is shown for scale.

5 Discussion

Field observations, mapping, and morphometric analysis reveal that the clastic dike system and the Pratzim drainage network have similar geometric characteristics and spatial trends. These include the similar orientations of clastic dikes and tributaries (Figure 13), and the rectangularity of the Pratzim drainage network, with abundant right-angle tributary junctions and stream bends (Figure 14) that mirrors the dominance of right angles in cross-cutting dikes (Figure 15). Furthermore, many of the morphological features of the Pratzim canyon system in the central region, where clastic dikes are abundant, are unique. These include valleys with sub-vertical banks and heads, exceptionally small drainage area at several steep valley heads (Figure 6), flat valley bottoms, and trapezoid valley cross sections (Figure 5). Based on these observations, we proposed that Ami'az Plain presents a case where landscape evolution is controlled by geologic structures. Specifically, we propose that the clastic dikes dictate the 3D geometry of the Pratzim drainage network, in agreement with previous studies of rectangular drainage networks associated with fractures (Zernitz, 1932; Howard, 1967; Deffontaines and Chorowicz, 1991).

To explain how clastic dikes dictate the evolution of the drainage network in the Ami'az Plain, we developed a three-component, conceptual hydrologic-geomorphic process model that accounts for the prevalence of caves, sinkholes, courtyards, and rock bridges in close proximity to the drainage network (Figures 8 - 11), and the spatial relations between the clastic dikes and these morphological features. The first component invokes the tendency of clastic dikes to focus subsurface flow, which in turn induces internal erosion and forms pipe caves with outlets at canyon banks and heads. The second component includes seepage erosion at channel heads and courtyards together with collapse of cave roofs to form sinkholes and new courtyards. Coalescence of adjacent collapsed features generates new subaerial tributaries, and the exposure of clastic dikes along the banks and heads of the new tributaries activates them as preferential subsurface flow paths, feeding back into the first component. The third component is expressed by fluvial activity and bank collapse events along the Pratzim canyon system (i.e., fluvial morphological changes). Below, we discuss the three components in conjunction with the findings of the present study.

5.1 Subsurface flow along clastic dikes and pipe formation

The alternating aragonite and detritus varves of the Lisan formation together with the capping gypsum layer make the Lisan formation particularly impermeable for vertical infiltration. However, in places where clastic dikes penetrate the capping gypsum layer, dikes may provide preferred pathways for infiltration of surface runoff. Field observations (listed below) and our experimental results indicate that subsurface flow along the clastic dikes removes the dikes' infilling material and part of the bounding Lisan country rocks, leading to internal erosion and the forming pipe systems.

First, in Ami'az Plain and in other regions surrounding the Dead Sea, where clastic dikes penetrate the Lisan rocks, surface lineaments are observed above the dikes and are considered as their surface expression (Jacoby et al., 2015). As these lineaments are depressions, they likely represent missing material. Field observations shows that the missing material of the depressed lineaments was removed by internal erosion and transport. At early developmental stages, lineaments may appear as a series of small holes arranged in a linear trend with no surface drainage to transport the missing material (Figure 9b). At more advanced stages, the lineaments develop into small and shallow channel and canyons with a depth of up to 8 m. In some cases, these depressions lack surface drainage (Figure 9a), and in other cases, the lineaments can flow under rock bridges (Figure 9d).

Second, cave outlets along the canyon banks are dominantly located at or to the side of clastic dikes (Figure 10). Within large caves, we commonly observed dikes along the ceiling that follow the course of the caves (e.g. Figure 12). These findings suggest that the caves were formed by the removal of subsurface material along and adjacent to the dikes.

Third, the infiltrating water in the barren Ami'az Plain is expected to be poor in dissolved CO_2, reducing its aggressivity toward dissolving the Lisan formation rocks. This, together with the observation that caves gradually grade toward their outlets at tributaries banks and heads indicate that the Pratzim caves are dominantly formed by internal erosion and piping rather then by karst processes.

Fourth, the dikes infilling material and the Lisan rocks are prone for piping. The outcomes of our field experiments showed that porous flow within a dike infilling material could generate a macro pipe through internal erosion, as indicated by the expulsion of muddy fluid during the experiments. Furthermore, the inlet of the experimental pipe had a keyhole-shape cross section, and it formed in two consecutive stages. Initially, with circular cross section, and then, the rectangular base was incised by the flowing water that remained in the experimental pool. The morphological similarity between the experimental pipe inlet and the keyhole-shape cross section of natural caves in Ami'az Plain, including the Flour Cave (Figure 12), supports the mechanistic similarity between the processes that formed the experimental pipe and natural pipe formation along dikes.

Generally, the susceptibility of the Lisan lithology to develop pipes is widely seen in the secondary pipe caves that cut through collapsed bank material, which dams narrow tributaries (Figure 10c). Moreover, in a number of outcrops, caves develop alongside dikes, such that the infilling material and the dike plain are partly preserved. Based on these observations, we propose that the Lisan country rocks have an equal or even higher susceptible to internal erosion and pipe formation than that of the dikes infilling material, and the interface between the dikes and the Lisan host rocks, may focus subsurface flow more easily than the infilling material of the dike. Notwithstanding, the dikes are critical to facilitate vertical infiltration from the level of Ami'az Plane.

The relations between joints (clastic dikes are mode-I fractures) and pipe formation has been extensively discussed before (Parker, 1963; Howard, 1990; Parker and Higgins, 1990; Hagerty, 1991; Calvo-Cases and Harvey, 1996; Jones et al., 1997; Torri and Brya, 1997; Farifteh and Soeters, 1999; Lazzari et al., 2006; Xu et al., 2011; Bernatek-Jakiel and Poesen, 2018). Some of these studies specifically emphasized the role of joints in increasing water infiltration to the subsurface, generating preferential subsurface flow pathways, and facilitating internal erosion and piping. However, unlike the pipes in Ami'az Plain, most of the pipes associated with joints form in soils, and their diameter is commonly up to tens of centimeters. Uniquely, Farifteh and Soeters (1999) reported on large scale pipes, with a width of up to two meters, that formed along tectonic joints in marly-clay marine sediments, resembling in dimensions the pipe caves in Ami'az Plain.

5.1.1 The mechanics of piping along clastic dikes in Ami'az Plain

We propose that clastic dikes promote the formation and growth of pipe caves in Ami'az Plain through three stages. Initially, subsurface flow through the dike infilling material could be characterized as a porous flow that is capable of gradually removing particles. This stage was observed in the second, 'water level drop', field experiment, where muddy, particle-rich material flew out of the alcove. The exponential fit to the water level drop trend that could be well-explained by a simple model of flow through porous media (Figure 16) indicates that during these initial stages, porous flow is the dominant process. Then, the classic mechanism of pipe growth applies, whereby a pressure gradient across a pipe promotes a relatively rapid flow that exerts shear stresses on the walls of the pipe. When the shear stresses surpass the cohesion and the shear resistance of the wall material, the flowing water detaches particles from the wall and transports them with the flow. Particle detachment and transport enlarge the pipe diameter (Parker, 1963; Parker and Higgins, 1990), which could lead to a pipe growth instability.

Assuming that the pressure gradient across the pipe, $\Delta P/l$ [Pa/m] is time-invariant, where l is the length of the pipe, and that the flow is laminar, the shear stress, τ [Pa] on the pipe walls can be expressed as (Turcotte and Schubert, 2002):

$$\tau = \frac{R(t)}{2}\frac{\Delta P}{l}, \tag{6}$$

Where $R(t)$ [m] is the radius of the pipe at time t [s]. Bonelli and Brivois (2008) proposed a simple shear stress dependent pipe erosion law of the form:

$$\frac{dR(t)}{dt} = \begin{cases} K(\tau - \tau_c), & \tau > \tau_c \\ 0, & \text{otherwise} \end{cases} \tag{7}$$

where K [m s^{-1} Pa^{-1}] is an erodibility coefficient and τ_c is a critical shear stress, below which erosion cannot take place. Combining equations (6) and (7) leads to:

$$\frac{dR(t)}{dt} = \begin{cases} K\left(\frac{\Delta P}{2l}R(t) - \tau_c\right), & \frac{\Delta P}{2l}R(t) > \tau_c \\ 0, & \text{otherwise.} \end{cases} \tag{8}$$

The solution of equation (8) with the initial condition $R(t=0) = R_0$ and assuming that $R_0 \Delta P/2l = \tau_0 > \tau_c$ is

$$R(t) = R_0 \frac{\tau_c}{\tau_0} + R_0 \left(1 - \frac{\tau_c}{\tau_0}\right) \exp\left(\frac{K\tau_0}{R_0} t\right). \tag{9}$$

Equation (9) reveals that when the initial pipe radius is sufficiently large to erode the walls, the pipe radius experience an exponential growth in time. Such an exponential growth probably controlled the extremely rapid formation of the macro pipe that terminated the third, 'constant water level' experiment. In the case of the montmorillonite rich Lisan lithology (Arkin and Michaeli, 1986), particle detachment from the walls could be assisted by dispersion of aggregates (Parker, 1963), which is commonly associated with piping (Bernatek-Jakiel and Wrońska-Wałach, 2018) and is expected to reduce τ_c.

Finally, the exponential rapid growth is expected to terminate when the pipe is too large to be fully occupied by water during flow events. Subsequent flows would therefore erode the pipe base, similar to subaerial fluvial erosion, and blocks from the pipe walls and ceiling would collapse and enlarge the pipe sideways and upward.

5.2 Pipe collapse and seepage erosion form and extend tributaries

Many of the large sinkholes in the study area are connected to the Pratzim drainage network through pipe caves. The association between sinkholes and pipe caves in known from other field areas (Parker, 1963; Parker and Higgins, 1990; Higgins and Schoner, 1997; Zhu, 2012; Bernatek-Jakiel and Wrońska-Wałach, 2018) and is related to local collapses of caves roof (Parker, 1963; Parker and Higgins, 1990; Bernatek-Jakiel and Wrońska-Wałach, 2018). In some of the sinkholes in Ami'az Plain, the collapsed material still fills the sinkhole, and occasionally, secondary pipes form through the collapsed material parallel to the course of the cave. Importantly, we observed numerous cases were several sinkholes form along a single pipe in close proximity to one another, such that they are fully connected at the subsurface, and only narrow rock bridges separate them (Figure 18).

Courtyards likely form by a similar process of cave roof collapse, occurring immediately at the cave outlet. The collapsed material still blocks many of the courtyards, forcing the drainage through secondary pipes that develop in the collapsed material. Observations of caves that extend inward from the courtyards support the link between courtyards and cave collapse.

We propose that in the central region of Ami'az Plain, new tributaries form by coalescence of sinkholes and courtyards, and generally by the collapse of pipe caves. A critical observation for this process was identified in several key sites, where only narrow rock bridges separate elongated, tributary-like sinkholes from the main tributaries to which they drain (Figure 11, and supplementary movie). If the rock bridges collapse, the resultant morphology would not be indistinguishable from other tributaries in the region.

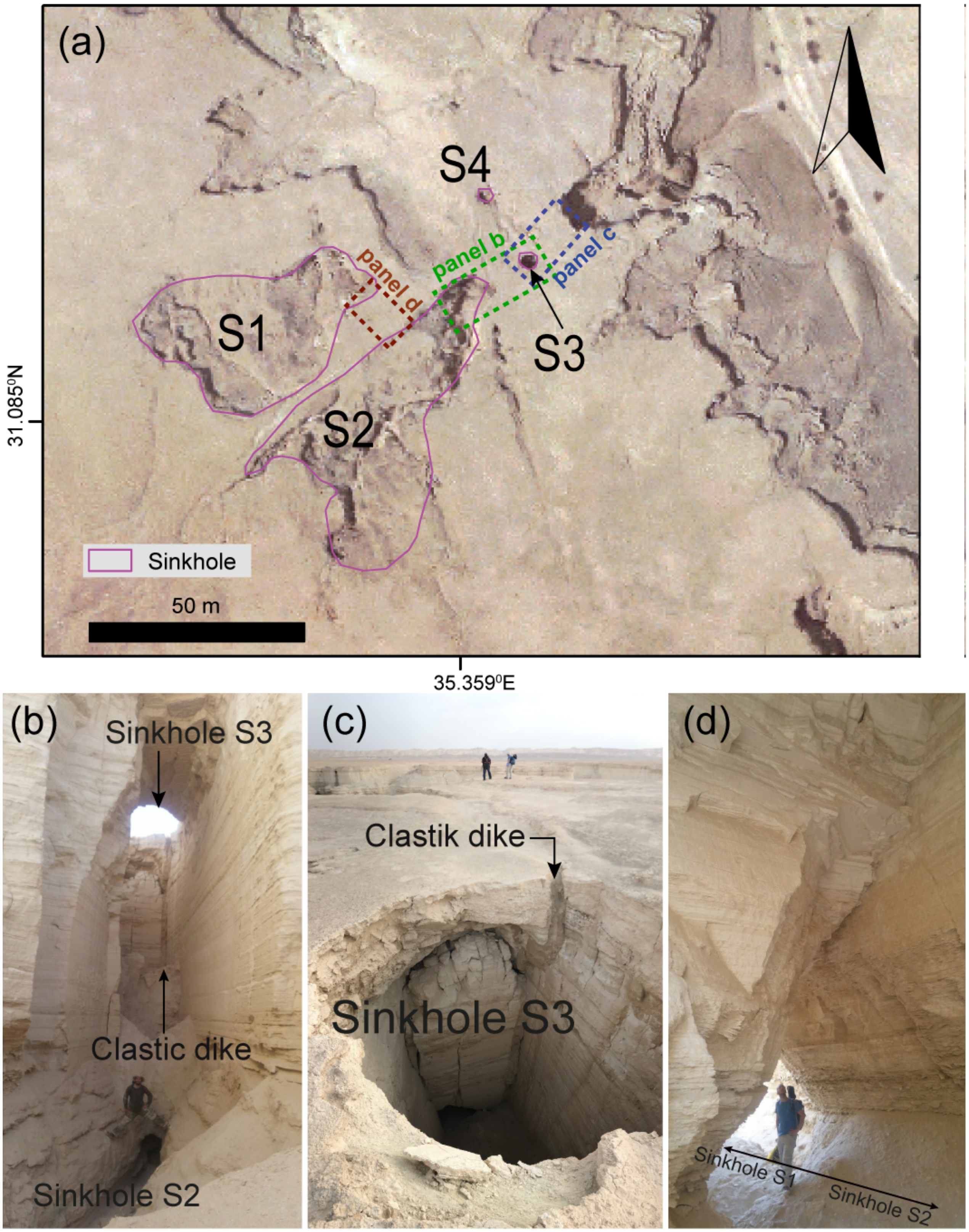

Figure 18: (a) A system of four sinkholes, S1 - S4 connected at the subsurface by a system of pipe caves. Dashed rectangles mark the location of the pictures in panels (b) - (d). (b) A pipe cave that preserves the flat plain of a clastic dike connecting sinkholes S2 and S3. (c) View of sinkhole S3 showing the filled dike along which the pipe in (b) developed. (d) A pipe cave connecting sinkholes S1 and S2.

Parallel to the process of cave roof collapse, we propose that tributaries in the central region extend backward by seepage erosion along canyon heads that undercuts and topples material above the seepage point. A common observation is collapsed cliff material that accumulates and blankets canyon heads, forcing the active channel to meander in between aprons or flow through the collapsed material in secondary pipes. Observations of clastic dikes and small cave outlets at canyon heads suggest that subsurface flow toward seepage points is routed along these structures. Seepage erosion likely formed the alcove following the first field experiment and extended it backward during the second experiment. Courtyards could play a similar role to channel heads and extend backward by seepage erosion, forming new tributaries. Where courtyards are close to channel heads, their backward extension could form bends along the tributaries.

The role of seepage erosion in carving deep canyons in soft lithologies has been demonstrated in experiments (e.g. Howard and McLane, 1988) and was invoked in various field settings (Higgins, 1982; Laity and Malin, 1985; Schumm et al., 1995; Micallef et al., 2020). The role of seepage erosion in creating similar morphologies in hard bedrock is, however, still debated (Lamb et al., 2006). The Lisan formation, although formally a bedrock, represents a soft end-member. Importantly, while seepage erosion is commonly associated with continuous subsurface flow below the water table (Dunne, 1980; Dunne et al., 1990; Laity and Malin, 1985; Schumm et al., 1995; Lamb et al., 2006; Pelletier and Baker, 2011; Micallef et al., 2020), in Ami'az Plain, the water table is deeper than the base of the tributaries and seepage erosion probably occurs during scarce and large rainfall events. Indeed, several morphologies that are commonly associated with seepage erosion are widely seen in the central region of Ami'az Plain, these include amphitheater valley heads, steep channel banks, and an approximately constant valley width (Laity and Malin, 1985; Schumm et al., 1995; Micallef et al., 2020, and references therein). We propose that indistinguishable morphologies emerge also when tributaries form by pipe caves collapse.

5.3 Morphological modifications of subaerial tributaries

When a new tributary or a tributary-like sinkhole forms by coalescence of collapse structures, fluvial erosion modifies the tributary shape. A meandering channel forms that flows along the valley bottom and transports away the eroded and collapsed material. In parallel, tributary valley widens by bank collapse. Occasionally, large blocks detach from the bank and tilt against it. More commonly, smaller bank collapse events are assisted by the presence of bank-parallel joints that likely form by topographic stresses (e.g. Molnar, 2004). When the tributary is narrow, the collapsed bank material blocks subaerial flow pathways. In these cases, the characteristic varves of the Lisan formation are seen folded and tilted over on top of the valley floor, creating the lows-and-highs morphology (Figure 5d). In these locations, secondary pipes cut through the collapsed material forming a continuous flow pathway (Figure 10c). Some wide tributaries preserve older collapse features, whereby terraces alongside of the meandering active channel show horizontal varves capped by fluvial deposit, overtopped by tilted and folded varves (Figure 19). Despite fluvial modification and bank collapse events, channels tend to preserve their linear valley-base grading and uniform canyon width along any single tributary.

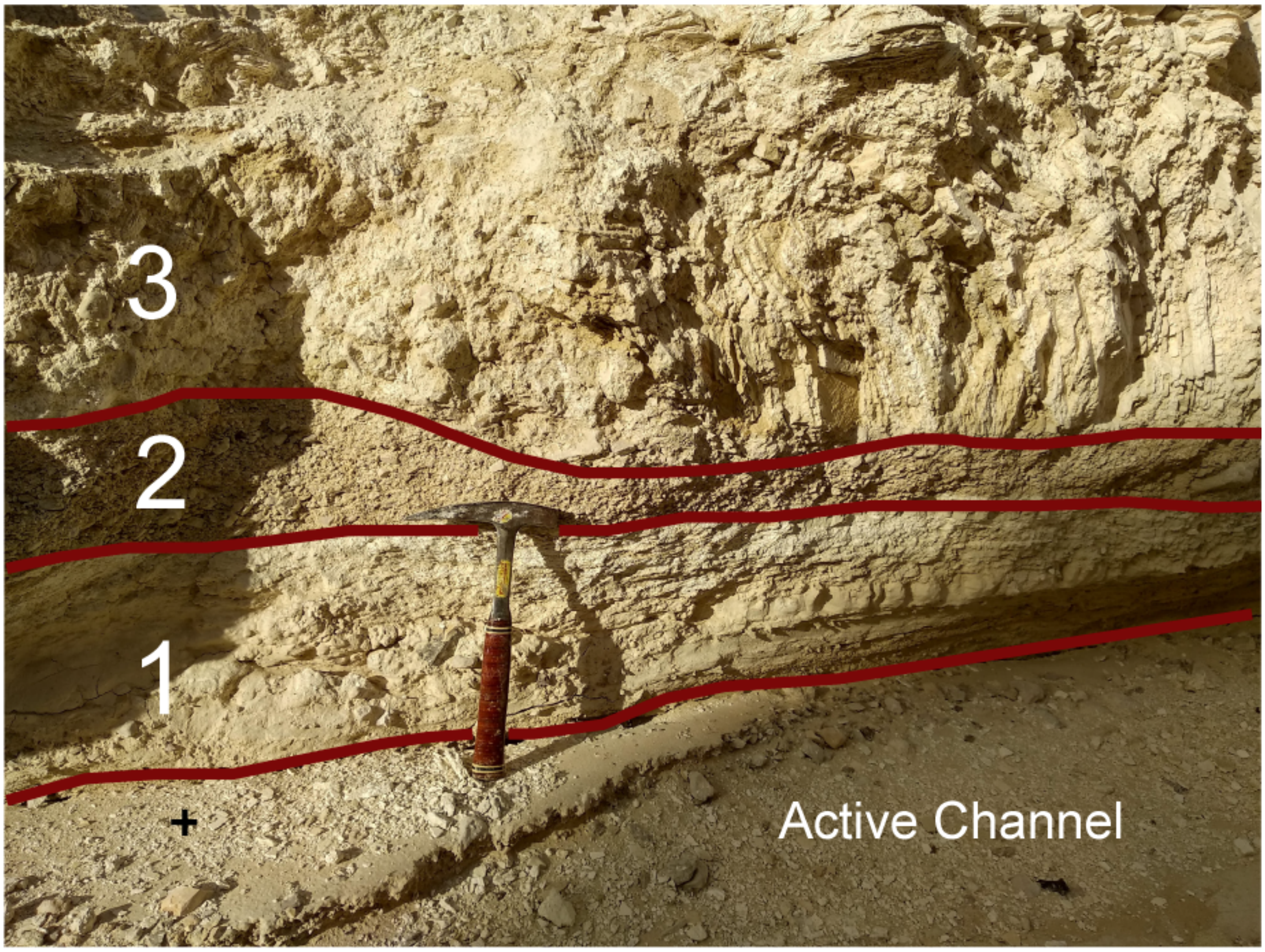

Figure 19: Stratigraphy of a terrace to the side of an active channel. Laminar varves of the Lisan country rocks at the base (1), a layer of mixed-grain deposit at the middle (2), and a layer of collapsed folded varves (3). Black + symbol coordinates area 31.0825 N, 35.3513 E.

5.4 Implications for landscape evolution

The hydrologic-geomorphic process model presented here implies that in the central region of Ami'az Plain, internal erosion (piping) and seepage erosion dictate the course of the drainage network by forming new tributaries and extending existing ones toward the undissected sections of Ami'az Plain. Fluvial erosion and bank collapse become important after tributaries form and extend by cave collapse and seepage erosion. Several attributes of the region decrease the efficiency of subaerial fluvial incision with respect to internal erosion in setting the course of drainage lines. First, the small drainage area inhibits significant surface runoff, particularly along channel heads (Figure 6). Second, the low erodibility of the surface of Ami'az Plain, which is protected by a gypsum layer, and the general lack of erosive tools (namely, hard grains) capable of abrading the gypsum layer hinders surface incision. Third, the exceptional low grading of Ami'az Plain increases the infiltration potential and decreases the shear stress of the flowing surface water.

Unlike the central region, the western region of the study area exhibits a dendritic drainage pattern with channels that gradually grade from the level of Ami'az Plain (i.e., tributaries lack cliff-dominated, amphitheater channel heads) (Figure 5b). In the western region, fluvial incision appears to play a dominant role in carving the channels. Its relative efficiency is probably assisted by the streams that drain sections of the Judea foothills and over to the Ami'az Plain. These streams supply abundant carbonate clasts that act as incision tools and possibly a greater stream power due to the topographic gradient across the fault.

Since the central region is significantly larger than the western region, our analysis indicates that internal erosion and cave collapse generally dominate the landscape evolution in the Ami'az Plain. The efficiency of landscape evolution in Ami'az Plain could be demonstrated not only locally, but also on a regional scale. Approximately 15 km south of the study area, within the Lisan formation, Davis et al. (2009) estimated fluvial incision rate of 0.64 - 1.15 mm/yr since $13.1 - 21.8$ Kyr to the present. This value is smaller than the average Holocenic erosion rate of $1.54 - 1.84$ mm/yr estimated in the current study for the canyon system in Ami'az Plain. Furthermore, Davis et al. (2009) study area was close to the outlet of Wadi Zin near the Dead Sea, where the upstream drainage area of Wadi Zin is ~ 1400 km^2, larger by three to four orders of magnitude than that of the Ami'az Plain, making the erosion rate in Wadi Pratzim exceptional.

The positive feedback between internal erosion and landscape evolution that lies at the heart of the proposed hydrologic-geomorphic process model predicts that the Pratzim drainage network expands outward. More specifically, the model posits that the exposure of clastic dikes along the banks and heads of newly formed tributaries promotes internal erosion along and to the side of these dikes that, in turn, generates newer tributaries. This feedback is seen in the density analysis of collapse related landforms (Figure 7b), showing that sinkholes and courtyards are concentrated in the periphery of the central region and particularly proximal to remote tributaries and steep channel heads. The model therefore predicts the future trajectory of landscape evolution in Ami'az Plane, whereby the cave and sinkhole system will continue to develop within and beyond the study area, with a gradual expansion of the drainage system toward the undissected eastern and southern regions of Ami'az Plain. Formation of new caves could potentially increase collapse related hazard.

Pipe formation by internal erosion is more commonly associated with soils, terraces and embankment dams (e.g. Bernatek-Jakiel and Wrońska-Wałach, 2018). The large scale, widespread and deep piping that cut through the Lisan formation rocks in the Ami'az Plain to form deep canyons adds to the natural landscape domains where internal erosion occurs and pipe caves form.

Finally, we note that the mechanistic association we identified between a rectangular drainage network with deep canyons and vertical walls, together with proximal sinkholes and caves, on the one hand, and a large scale orthogonal system of fractures (clastic dikes in the our study area), on the other hand, could be applicable across other terrestrial and planetary rectangular drainages. More specifically, identifying rectangular drainages associated with large-scale orthogonal tectonic fabric over terrestrial and planetary surfaces, particularly, if the surfaces are relatively planar and proximal sinkholes are observed, could be indicative to the presence of large sub-surface voids, i.e., caves.

6 Summary

Detailed morphometric analysis of the drainage system of Wadi Pratzim that incises into Ami'az Plain shows a rectangular drainage pattern dominated by right angle confluences and bends. The similar orientation of drainage lines and surface lineaments, together with field observations of clastic dikes at channel heads indicate that the rectangular drainage developed in association with locally sub-orthogonal sets of clastic dikes. Along the central region of the study area, the canyon system is characterized by a relatively flat bed, an approximately constant width along any given tributary, and steep, subvertical, banks and valley heads, draining, in some cases, a surprising small drainage area. These unique morphologies add to the many sinkholes around the canyon system and pipe caves that drain to the canyon system, both are spatially associated with clastic dikes.

These observations indicate that the Pratzim drainage network is structurally controlled by a locally sub-orthogonal system of clastic dikes. We develoedp a hydrologic-geomorphic conceptual process model that explains the development of the rectangular drainage pattern in association with the clastic dikes, and the formation of pipe caves and sinkholes. The model invokes (1) Subsurface flow along clastic dikes that act as preferred flow pathways. Subsurface flow induces internal erosion, forming and enlarging pipe caves, as supported by a series of field experiments that demonstrated the feasibility of pipe formation along a clastic dike. (2) When cave roofs collapse sinkholes form. Coalescence and merging of sinkholes form new tributaries. Key indicators for this stage are narrow rock bridges that separate elongated sinkholes from the Pratzim tributaries in multiple locations. The sinkholes drain to the tributaries under the bridges, and upon bridge collapse new tributaries will be formed. Additionally, seepage erosion at channel heads (above the water table) extends existing tributaries. (3) Fluvial erosion and bank block collapse modify the morphology of newly formed tributaries. Clastic dikes exposed along newly formed pipe caves and tributaries refocus subsurface flow and allow the landscape to continue to evolve by the same process.

The conceptual model implies that internal erosion dominates over fluvial erosion in setting the geometry of the Pratzim drainage network. A calculation based on the volume of the missing material from the canyon system reveals an average erosion rate of $1.54 - 1.84$ mm/yr over the Holocene. This high rate despite the notable small drainage area of several km^2 and the flatness of Ami'az Plain implies that subsurface erosion is remarkably efficient in forming the drainage netwrok in this hyper arid region.

The evident association found between the rectangular drainage pattern and orthogonal fracture sets, which is mediated by a system of caves and subsurface cavities could be applicable across other terrestrial and planetary rectangular drainage systems. We, therefore, suggest that rectangular systems associated with an orthogonal fabric and proximal sinkholes should be considered as a location were caves could be abundant.

A Appendix: Experimental Observations

Here, we detail our experimental observations of flow out of the alcove and morphological changes.

Table A1: Observations from the second, 'water level drop' experiment

Time[†][s]	Water level [cm]	Observations
0	11.5	No flow
49	11	No flow
153	10	Muddy fluid starts flowing along the base of the alcove from the far tip of the alcove toward the cliff
370	9	Flow flux increases
629	8	Flow continues
878	7	No flow
1004	6.5	No flow
1222	6	No flow
1516	5	No flow
1807	4.3	No flow

[†] Time from the onset of the experiment

Table A2: Observations from the third, 'constant water level' experiment

Time[†][s]	Water level [cm]	Observations
0	12	-
93	11.5	Pulse of fluid along the dike front approximately at the center of the alcove.
109	12	Another pulse of fluid along the center of the alcove
124	12	Another pulse of fluid along the center of the alcove.
136	12	Flow seeps out at a new location in the dike front.
180	12	Flow continues along two pathways
192	12	Flow continues along two pathways. Dike particles from the alcove walls fall down.
225	12	Flow continues along two pathways.
269	12	Flow continues along two pathways. Fluid flux increases.
324	12	Strong flow pulse along the original pathways. Second pathway is still active.
505	13	Rapid flow along the two pathways with material removal.
1002	19	A new pathway appears, and flow occurs along the three pathways. Dike material continues to collapse.
1197	19	Flow continues and incision at the base of the first pathway is visible.
1272	19	Significant removal from dikes filling material is distinct.
2037	19	Flow continues. Visible subsidence of the surface above the alcove, between the experimental pool and the cliff.
2080	19	Abrupt formation of a pipe that connects the experimental pool to the alcove and the cliff. Pipe average radius of 6 cm. The water from the experimental hole quickly drains through the pipe. The pipe base is incised by the flow and drains the remaining water in the experimental pool.

† Time from the onset of the experiment

Acknowledgments

This research was supported by the ISRAEL SCIENCE FOUNDATION (grant No. 562/19), and by a grant from the Israeli Government under Geological Survey of Israel DS project 70734. The authors thank A. Frumkin and B. Langford for insightful discussions of pipe caves in the Dead Sea Basin. B. Langford and E. Harel are thanked for field assistant. R. Rosenzweig and J. Laronne are thanked for field equipment.

Author Contributions

MH - (c), (d), (f), (i)
LG - (a), (b), (c), (d), (f), (g), (h), (i)
TL - (b), (c), (d),(g), (i)
AM - (b), (c),(d), (e), (g), (i)
The authors declare no conflict of interest.

Data Availability Statement

The data generated and used in the analysis presented here is available in the supplementary information attached to this manuscript.

References

Abrahams, A. D. and Flint, J. J., 1983. Geological controls on the topological properties of some trellis channel networks (in the Appalachians). *Geological Society of America Bulletin*, 94(1):80–91. 10.1130/0016-7606(1983)94¡80:GCOTTP¿2.0.CO;2.

Anton, L., Mather, A. E., Stokes, M., Muñoz-Martin, A., and De Vicente, G., 2015. Exceptional river gorge formation from unexceptional floods. *Nature Communications*, 6(1):7963. 10.1038/ncomms8963.

Argialas, D. P., Lyon, J. G., and Mintzer, O. W., 1988. Quantitative description and classification of drainage patterns. *Photogrammetric Engineering & Remote Sensing*, 54(4): 505–509.

Arkin, Y. and Michaeli, L., 1986. The significance of shear strength in the deformation of laminated sediments in the Dead Sea area. *Israel Journal of Earth-Sciences*, 35(2):61–72.

Bernatek-Jakiel, A. and Poesen, J., 2018. Subsurface erosion by soil piping: significance and research needs. *Earth-Science Reviews*. 10.1016/j.earscirev.2018.08.006.

Bernatek-Jakiel, A. and Wrońska-Wałach, D., 2018. Impact of piping on gully development in mid-altitude mountains under a temperate climate: A dendrogeomorphological approach. *CATENA*, 165:320–332. https://doi.org/10.1016/j.catena.2018.02.012.

Bonelli, S. and Brivois, O., 2008. The scaling law in the hole erosion test with a constant pressure drop. *International Journal for Numerical and Analytical Methods in Geomechanics*, 32(13):1573–1595. 10.1002/nag.683.

Burr, D. M., Jacobsen, R. E., Roth, D. L., Phillips, C. B., Mitchell, K. L., and Viola, D., 2009. Fluvial network analysis on Titan: Evidence for subsurface structures and west-to-east wind flow, southwestern Xanadu. *Geophysical Research Letters*, 36(22):1–5. 10.1029/2009GL040909.

Burr, D. M., Drummond, S. A., Cartwright, R., Black, B. A., and Perron, J. T., 2013. Morphology of fluvial networks on Titan: Evidence for structural control. *Icarus*, 226(1): 742–759. 10.1016/j.icarus.2013.06.016.

Calvo-Cases, A. and Harvey, A. M., 1996. Morphology and development of selected badland in southeast Spain. *Earth Surface Processes and Landforms*, 21(8):725–735. 10.1002/(SICI)1096-9837(199608)21:8¡725::AID-ESP642¿3.0.CO;2-V.

Campbell, M. R., 1896. Drainage Modifications and Their Interpretation. *The Journal of Geology*, 4(5):567–581. 10.1086/607555.

Davis, M., Matmon, A., Zilberman, E., Porat, N., Gluck, D., and Enzel, Y., 2009. Bathymetry of Lake Lisan controls late Pleistocene and Holocene stream incision in response to base level fall. *Geomorphology*, 106(3):352 – 362. https://doi.org/10.1016/j.geomorph.2008.11.014.

Deffontaines, B. and Chorowicz, J., 1991. Principles of drainage basin analysis from multi-source data: Application to the structural analysis of the Zaire Basin. *Tectonophysics*, 194 (3):237–263. https://doi.org/10.1016/0040-1951(91)90263-R.

Devauchelle, O., Petroff, A. P., Seybold, H. F., and Rothman, D. H., 2012. Ramification of stream networks. *Proceedings of the National Academy of Sciences*, 109(51):20832–20836. 10.1073/pnas.1215218109.

Dunne, T., 1980. Formation and controls of channel networks. *Progress in Physical Geography*, 4(2):211–239. 10.1177/030913338000400204.

Dunne, T. et al. Hydrology, mechanics, and geomorphic implications of erosion by subsurface flow. In *Groundwater Geomorphology: The Role of Subsurface Water in Earth-Surface Processes and Landforms*, volume 252, pages 1–28. Special Paper - Geological Society of America, 1990.

Duvall, A. R., Harbert, S. A., Upton, P., Tucker, G. E., Flowers, R. M., and Collett, C., 2020. River patterns reveal two stages of landscape evolution at an oblique convergent margin, Marlborough Fault System, New Zealand. *Earth Surface Dynamics*, 8(1):177–194. 10.5194/esurf-8-177-2020.

Farifteh, J. and Soeters, R., 1999. Factors underlying piping in the Basilicata region, southern Italy. *Geomorphology*, 26(4):239 – 251. https://doi.org/10.1016/S0169-555X(98)00070-1.

Garfunkel, Z., Zak, I., and Freund, R., 1981. Active faulting in the Dead Sea rift. *Tectonophysics*, 80(1):1–26. https://doi.org/10.1016/0040-1951(81)90139-6.

Haase-Schramm, A., Goldstein, S. L., and Stein, M., 2004. U-Th dating of Lake Lisan (late Pleistocene dead sea) aragonite and implications for glacial east Mediterranean climate change. *Geochimica et Cosmochimica Acta*, 68(5):985–1005. 10.1016/j.gca.2003.07.016.

Hagerty, D. J., 1991. Piping/Sapping Erosion. I: Basic Considerations. *Journal of Hydraulic Engineering*, 117(8):991–1008. 10.1061/(ASCE)0733-9429(1991)117:8(991).

Higgins, C. G., 1982. Drainage systems developed by sapping on Earth and Mars. *Geology*, 10(3):147–152. 10.1130/0091-7613(1982)10¡147:DSDBSO¿2.0.CO;2.

Higgins, C. G. and Schoner, C., 1997. Sinkholes formed by piping into buried channels. *Geomorphology*, 20(3-4):307–312. 10.1016/s0169-555x(97)00031-7.

Howard, A. D., 1990. Case study: Model studies of ground-water sapping. *Geol. Soc. Am. Spec. Pap*, 252:257–264.

Howard, A. D. and McLane, C. F., 1988. Erosion of cohesionless sediment by groundwater seepage. *Water Resources Research*, 24(10):1659–1674. 10.1029/WR024i010p01659.

Howard, A. D., 1967. Drainage analysis in geologic interpretation; a summation. *The American Association of Petroleum Geologists Bulletin*, 51(11):2246–2259.

Ichoku, C. and Chorowicz, J., 1994. A numerical approach to the analysis and classification of channel network patterns. *Water Resources Research*, 30(2):161–174. 10.1029/93WR02279.

Jacoby, Y., Weinberger, R., Levi, T., and Marco, S., 2015. Clastic dikes in the Dead Sea basin as indicators of local site amplification. *Natural Hazards*, 75(2):1649–1676. 10.1007/s11069-014-1392-0.

Jones, J. A. A., Richardson, J. M., and Jacob, H. J., 1997. Factors controlling the distribution of piping in Britain: a reconnaissance. *Geomorphology*, 20(3):289–306. https://doi.org/10.1016/S0169-555X(97)00030-5.

Jung, K., Marpu, P. R., and Ouarda, T. B. M. J., 2015. Improved classification of drainage networks using junction angles and secondary tributary lengths. *Geomorphology*, 239:41–47. https://doi.org/10.1016/j.geomorph.2015.03.004.

Jung, K., Marpu, P. R., and Ouarda, T. B. M. J., 2017. Impact of river network type on the time of concentration. *Arabian Journal of Geosciences*, 10(24):546. 10.1007/s12517-017-3323-3.

Jung, K., Shin, J.-y., and Park, D., 2019. A new approach for river network classification based on the beta distribution of tributary junction angles. *Journal of Hydrology*, 572 (February):66–74. 10.1016/j.jhydrol.2019.02.041.

Kemp, J. Preliminary report on the geology of Essex County. Technical report, New York State Mus. Ann. Rept, 1894.

Khawja, S., Ernst, R. E., Samson, C., Byrne, P. K., Ghail, R. C., and MacLellan, L. M., 2020. Tesserae on venus may preserve evidence of fluvial erosion. *Nature Communications*, 11(1):5789. 10.1038/s41467-020-19336-1.

Komatsu, G., Gulick, V. C., and Baker, V. R., 2001. Valley networks on Venus. *Geomorphology*, 37(3):225–240. https://doi.org/10.1016/S0169-555X(00)00084-2.

Laity, J. E. and Malin, M. C., 1985. Sapping processes and the development of theater-headed valley networks on the Colorado Plateau. *GSA Bulletin*, 96(February):203–217. 10.1130/0016-7606(1985)96¡203.

Lamb, M. P., Howard, A. D., Johnson, J., Whipple, K. X., Dietrich, W. E., and Perron, J. T., 2006. Can springs cut canyons into rock? *Journal of Geophysical Research E: Planets*, 111 (7):1–18. 10.1029/2005JE002663.

Lazzari, M., Geraldi, E., Lapenna, V., and Loperte, A., 2006. Natural hazards vs human impact: an integrated methodological approach in geomorphological risk assessment on the Tursi historical site, Southern Italy. *Landslides*, 3(4):275–287. 10.1007/s10346-006-0055-y.

Levi, T. Weinberger, R., Eyal, Y., and Marco, S. Clastic dikes in Ami'az Plain. In *the Annual Meeting of the Israeli Geological Society, En Bokek, Field guides book*, pages 61–76, 2014.

Levi, T., Weinberger, R., Aïfa, T., Eyal, Y., and Marco, S., 2006a. Earthquake-induced clastic dikes detected by anisotropy of magnetic susceptibility. *Geology*, 34(2):69–72. 10.1130/G22001.1.

Levi, T., Weinberger, R., Aïfa, T., Eyal, Y., and Marco, S., 2006b. Injection mechanism of clay-rich sediments into dikes during earthquakes. *Geochemistry, Geophysics, Geosystems*, 7(12). 10.1029/2006GC001410.

Levi, T., Weinberger, R., and Eyal, Y., 2011. A coupled fluid-fracture approach to propagation of clastic dikes during earthquakes. *Tectonophysics*, 498(1-4):35–44. 10.1016/j.tecto.2010.11.012.

Marco, S., Weinberger, R., and Agnon, A., 2002. Radial clastic dykes formed by a salt diapir in the Dead Sea Rift, Israel. *Terra Nova*, 14(4):288–294. 10.1046/j.1365-3121.2002.00423.x.

Marco, S., Rockwell, T. K., Heimann, A., Frieslander, U., and Agnon, A., 2005. Late Holocene activity of the Dead Sea Transform revealed in 3D palaeoseismic trenches on the Jordan Gorge segment. *Earth and Planetary Science Letters*, 234(1):189 – 205. https://doi.org/10.1016/j.epsl.2005.01.017.

Mejía, A. I. and Niemann, J. D., 2008. Identification and characterization of dendritic, parallel, pinnate, rectangular, and trellis networks based on deviations from planform self-similarity. *Journal of Geophysical Research: Earth Surface*, 113(2):1–21. 10.1029/2007JF000781.

Micallef, A., Marchis, R., Saadatkhah, N., Clavera-Gispert, R., Pondthai, P., Everett, M. E., Avram, A., Timar-Gabor, A., Cohen, D., Preca Trapani, R., and Weymer, B. A., 2020. Box canyon erosion along the Canterbury coast (New Zealand): A rapid and episodic process controlled by rainfall intensity and substrate variability. *Earth Surface Dynamics Discussions*, 2020:1–42. 10.5194/esurf-2020-29.

Molnar, P., 2004. Interactions among topographically induced elastic stress, static fatigue, and valley incision. *Journal of Geophysical Research: Earth Surface*, 109(F2). 10.1029/2003JF000097.

Molnar, P., Anderson, R. S., and Anderson, S. P., 2007. Tectonics, fracturing of rock, and erosion. *Journal of Geophysical Research: Earth Surface*, 112(F3). 10.1029/2005JF000433.

Nieber, J., Sidle, R., and Fox, G., 2013. Internal Erosion during Soil Pipeflow: State of the Science for Experimental and Numerical Analysis. *Transactions of the ASABE*, 56:465–478. 10.13031/2013.42667.

Parker, G. G. and Higgins, C. G., 1990. Piping and pseudokarst in drylands. *Special Paper - Geological Society of America*, 252:77–110. 10.1130/SPE252-p77.

Parker, G., 1963. Piping, a geomorphic agent in landform development of the drylands. *International Association of Scientific Hydrology Publication*, 65:103–113.

Pelletier, J. D. and Baker, V. R., 2011. The role of weathering in the formation of bedrock valleys on Earth and Mars: A numerical modeling investigation. *Journal of Geophysical Research E: Planets*, 116(11):1–13. 10.1029/2011JE003821.

Pelletier, J. D., Engelder, T., Comeau, D., Hudson, A., Leclerc, M., Youberg, A., and Diniega, S., 2009. Tectonic and structural control of fluvial channel morphology in metamorphic core complexes: The example of the Catalina-Rincon core complex, Arizona. *Geosphere*, 5(4): 363–384. 10.1130/GES00221.1.

Pillans, B., 1985. Drainage initiation by subsurface flow in South Taranaki, New Zealand. *Geology*, 13(4):262–265. 10.1130/0091-7613(1985)13¡262:DIBSFI¿2.0.CO;2.

Porat, N., Levi, T., and Weinberger, R., 2007. Possible resetting of quartz OSL signals during earthquakes—Evidence from late Pleistocene injection dikes, Dead Sea basin, Israel. *Quaternary Geochronology*, 2(1):272–277. https://doi.org/10.1016/j.quageo.2006.05.021.

Roy, S. G., Koons, P. O., Upton, P., and Tucker, G. E., 2015. The influence of crustal strength fields on the patterns and rates of fluvial incision. *Journal of Geophysical Research: Earth Surface*, 120(2):275–299. 10.1002/2014JF003281.

Schumm, S. A. and Phillips, L., 1986. Composite channels of the Canterbury Plain, New Zealand: A Martian analog? *Geology*, 14(4):326–329. 10.1130/0091-7613(1986)14¡326:CCOTCP¿2.0.CO;2.

Schumm, S. A., Boyd, K. F., Wolff, C. G., and Spitz, W. J., 1995. A ground-water sapping landscape in the Florida Panhandle. *Geomorphology*, 12(4):281–297. 10.1016/0169-555X(95)00011-S.

Scott, D. N. and Wohl, E. E., 2019. Bedrock fracture influences on geomorphic process and form across process domains and scales. *Earth Surface Processes and Landforms*, 44(1): 27–45. 10.1002/esp.4473.

Seybold, H., Rothman, D. H., and Kirchner, J. W., 2017. Climate's watermark in the geometry of stream networks. *Geophysical Research Letters*, 44(5):2272–2280. 10.1002/2016GL072089.

Sneh, A. and Weinberger, R. Major structures of israel and environs, scale 1:500,000. Geological Survey of Israel, 2014.

Torri, D. and Brya, R., 1997. Micropiping processes and biancana evolution in southeast Tuscany, Italy. *Geomorphology*, 20(3):219–235. https://doi.org/10.1016/S0169-555X(97)00025-1.

Turcotte, D. L. and Schubert, G., 2002. *Geodynamics*. Cambridge university press.

Twidale, C. R., 2004. River patterns and their meaning. *Earth-Science Reviews*, 67(3-4): 159–218. 10.1016/j.earscirev.2004.03.001.

Weinberger, R., Begin, Z. B., Waldmann, N., Gardosh, M., Baer, G., Frumkin, A., and Wdowinski, S., 2006a. Quaternary rise of the Sedom diapir, Dead Sea Basin. *Special Paper of the Geological Society of America*, 401(03):33–51. 10.1130/2006.2401(03).

Weinberger, R., Lyakhovsky, V., Baer, G., and Begin, Z. B., 2006b. Mechanical modeling and InSAR measurements of Mount Sedom uplift, Dead Sea basin: Implications for effective viscosity of rock salt. *Geochemistry, Geophysics, Geosystems*, 7(5). 10.1029/2005GC001185.

Weinberger, R., Bar-Matthews, M., Levi, T., and Begin, Z. B., 2007. Late-Pleistocene rise of the Sedom diapir on the backdrop of water-level fluctuations of Lake Lisan, Dead Sea basin. *Quaternary International*, 175(1):53–61. 10.1016/j.quaint.2007.03.007.

Whipple, K. X., Hancock, G. S., and Anderson, R. S., 2000a. River incision into bedrock: Mechanics and relative efficacy of plucking, abrasion, and cavitation. *GSA Bulletin*, 112 (3):490–503. 10.1130/0016-7606(2000)112¡490:RIIBMA¿2.0.CO;2.

Whipple, K. X., Snyder, N. P., and Dollenmayer, K., 2000b. Rates and processes of bedrock incision by the Upper Ukak River since the 1912 Novarupta ash flow in the Valley of Ten Thousand Smokes, Alaska. *Geology*, 28(9):835–838. 10.1130/0091-7613(2000)28¡835:RAPOBI¿2.0.CO;2.

Xu, L., Dai, F., Tham, L., Tu, X., Min, H., Zhou, Y., Wu, C., and Xu, K., 2011. Field testing of irrigation effects on the stability of a cliff edge in loess, North-west China. *Engineering Geology*, 120(1):10 – 17. https://doi.org/10.1016/j.enggeo.2011.03.007.

Zak, R. and Freund, R., 1980. Strain measurements in eastern marginal shear zone of Mount Sedom Salt Diapir, Israel. *American Association of Petroleum Geologists, Bulletin*, 64(4): 568–581. 10.1306/2f918a7c-16ce-11d7-8645000102c1865d.

Zernitz, E. R., 1932. Drainage Patterns and Their Significance. *The Journal of Geology*, 40 (6):498–521.

Zhu, T. X., 2012. Gully and tunnel erosion in the hilly Loess Plateau region, China. *Geomorphology*, 153-154:144–155. https://doi.org/10.1016/j.geomorph.2012.02.019.